

RESEARCH

Open Access



# Cerium-doped Prussian blue biomimetic nanozyme as an amplified pyroptosis inhibitor mitigate A $\beta$ oligomer-induced neurotoxicity in Alzheimer's disease

Jing Ma<sup>1,2,3†</sup>, Yu Tian<sup>1,2,3†</sup>, Chengzhong Du<sup>1,2,3†</sup>, Yang Zhu<sup>1,2,3</sup>, Wen Huang<sup>1,2,3</sup>, Chenyu Ding<sup>1,2,3</sup>, Penghui Wei<sup>1,2,3</sup>, Xuehan Yi<sup>4\*</sup>, Zhangya Lin<sup>1,2,3\*</sup> and Wenhua Fang<sup>1,2,3\*</sup>

## Abstract

Antioxidant enzyme therapy shows promise for treating Alzheimer's disease (AD), but significant challenges remain in achieving effective blood–brain barrier (BBB) penetration and sustained therapeutic effects. We developed a novel neutrophil membrane (NM)-coated cerium-doped Prussian blue biomimetic nanozyme (NM@PB-Ce) that demonstrates outstanding enzymatic properties and targeted therapeutic efficacy. Extensive physicochemical characterization using transmission electron microscopy, X-ray photoelectron spectroscopy, and dynamic light scattering confirmed the successful synthesis of uniform nanoparticles (~142 nm) with preserved membrane protein functionality. In vitro studies utilizing SH-SY5Y neuroblastoma cells revealed that NM@PB-Ce effectively scavenged reactive oxygen species through multiple enzyme-mimetic activities (catalase, superoxide dismutase, and peroxidase). The nanozyme significantly suppressed NLRP3 inflammasome activation and subsequent pyroptosis, reducing inflammatory markers (IL-1 $\beta$ , IL-18) while attenuating A $\beta$  aggregation. Using a sophisticated co-culture BBB model and real-time in vivo fluorescence imaging, we demonstrated NM@PB-Ce's ability to traverse the BBB and accumulate specifically in AD-affected regions. In an A $\beta$ 1-42 oligomer-induced AD mouse model, systematic administration of NM@PB-Ce (320  $\mu$ g/mL, 0.01 mL/g/day for 14 days) significantly improved cognitive performance across multiple behavioral paradigms, including the Morris water maze, Y-maze, and open field tests. Molecular and histological analyses revealed decreased neuroinflammation markers (GFAP, Iba-1) in the hippocampus, reduced levels of NLRP3, caspase-1, and phosphorylated tau (demonstrated by Western blot and ELISA), and enhanced dendritic spine density (visualized through Golgi staining). This comprehensive study establishes NM@PB-Ce as a promising therapeutic platform for AD treatment, providing both mechanistic insights into its mode of action and robust evidence of its therapeutic efficacy in targeting neuroinflammation and cognitive decline.

<sup>†</sup>Jing Ma, Yu Tian and Chengzhong Du have contributed equally to this work.

\*Correspondence:

Xuehan Yi

531154173@qq.com

Zhangya Lin

13799321745@139.com

Wenhua Fang

fang.wenhua@qq.com

Full list of author information is available at the end of the article

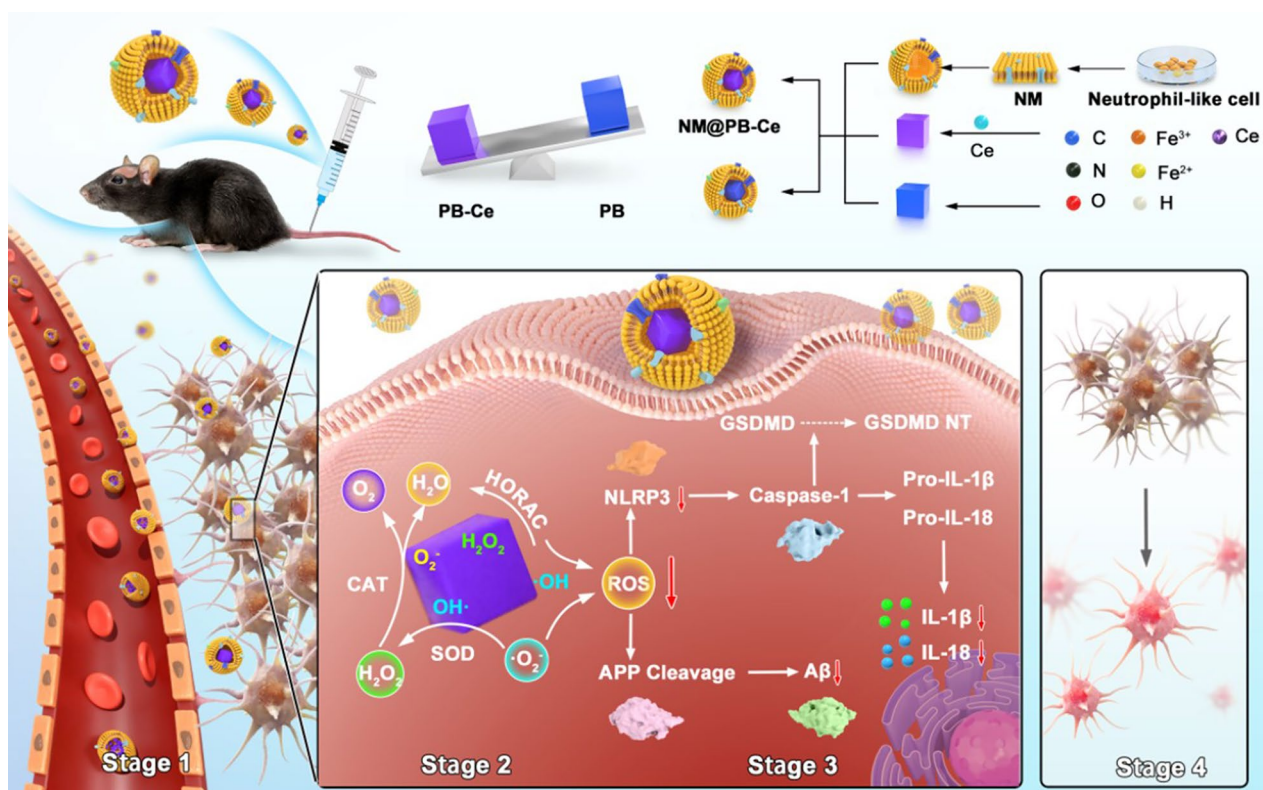


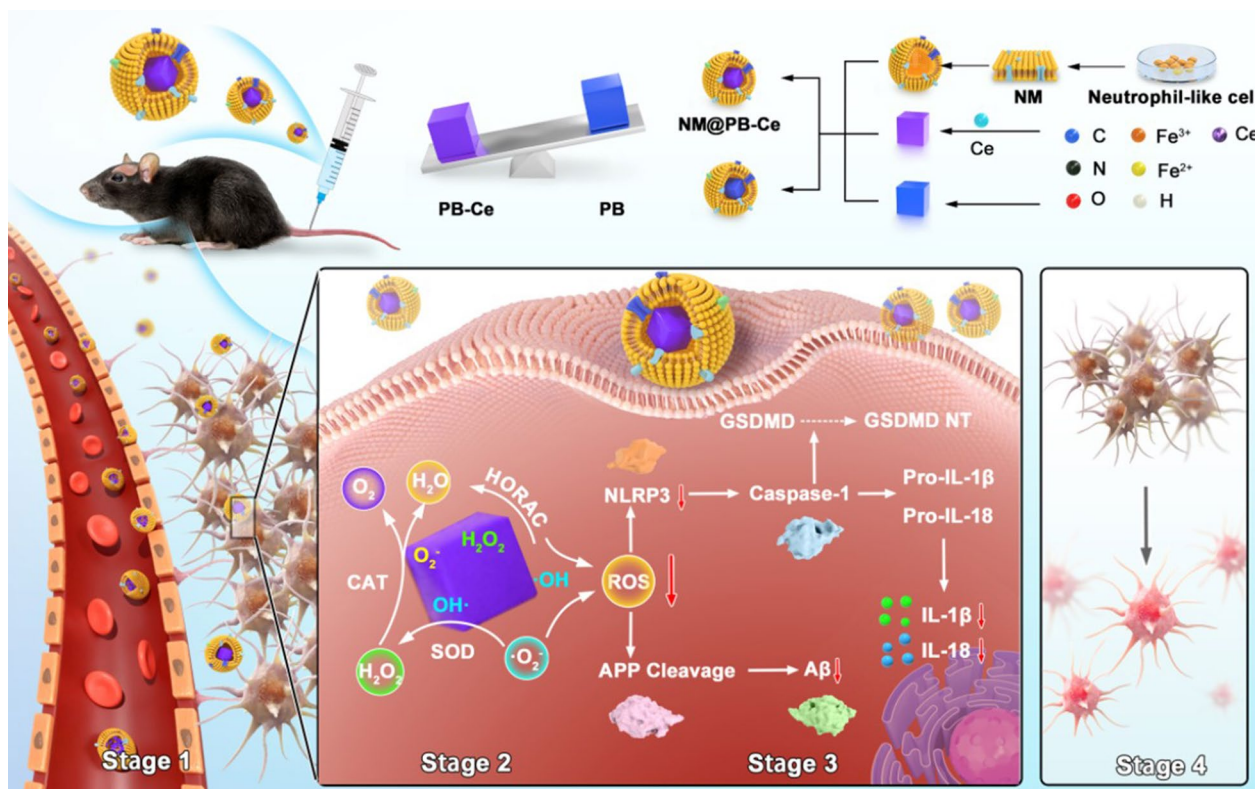
### Highlights

- NM@PB-Ce nanozyme crosses BBB to target AD regions with high enzymatic activity.
- The nanozyme reduces A $\beta$  neurotoxicity by scavenging ROS and inhibiting inflammation.
- NM@PB-Ce improves motor function and memory capabilities in AD mice models.
- It shows multiple protective effects by reducing tau phosphorylation and A $\beta$  aggregation.
- This platform provides new strategies for treating inflammation-related brain disorders.

**Keywords** Nanozyme, Alzheimer’s disease, Pyroptosis, Reactive oxygen species, Neuroinflammation

### Graphical Abstract





**Scheme 1** shows the synthetic process of biomimetic nanozymes. Schematic illustration of NM@PB-Ce nanozyme's therapeutic mechanism against Alzheimer's disease, demonstrating its capability to cross the blood–brain barrier via neutrophil membrane-mediated transport (Stage 1), followed by multiple enzyme-like activities (CAT, SOD, POD) that eliminate various ROS species (Stage 2). The cascade of therapeutic effects includes suppression of NLRP3 inflammasome activation, reduction of inflammatory factors, inhibition of pyroptosis, and decrease in Aβ accumulation (Stage 3), ultimately leading to reduced neuroinflammation and improved cognitive function (Stage 4). The top right panel details the composition and assembly of NM@PB-Ce, with color-coded elements: C (blue), Fe<sup>3+</sup> (orange), Ce (purple), N (black), Fe<sup>2+</sup> (yellow), O (red), and H (grey)

## Introduction

Alzheimer's disease (AD) is a devastating neurodegenerative disorder characterized by profound neurological and motor impairments, with hallmark pathological features including extracellular β-amyloid (Aβ) plaques and intracellular neurofibrillary tangles (NFTs) composed of hyperphosphorylated tau (P-tau) protein [1–3]. Historically considered incurable, there is an urgent need for effective therapeutic intervention [4–6]. Neuroinflammation, particularly that involving the NLRP3 inflammasome, has emerged as a critical factor in AD progression [7]. The NLRP3 inflammasome, a multiprotein complex comprising the NLRP3 sensor, ASC adaptor protein, and caspase-1 protease, assembles in response to various stimuli including bacterial toxins, oxidative stress, and Aβ aggregates [8, 9]. This assembly triggers caspase-1 activation and subsequent pyroptosis, exacerbating neuronal damage [10]. Elevated levels of interleukin (IL)–1β and IL-18 in patients with AD provide further evidence of significant neuroinflammation [11]. The established relationship between reactive oxygen species (ROS) and

NLRP3 inflammasome activation suggests that mitigating excessive mitochondrial ROS could attenuate oxidative damage, offering a potential strategy to inhibit NLRP3-mediated inflammatory responses and alleviate AD symptoms [12].

Compared with their natural enzyme counterparts, artificial nanozymes offer significant advantages, including enhanced catalytic activity, multifunctional enzyme-like properties, and superior stability, presenting novel opportunities for treating central nervous system disorders [13–15]. These nanozymes are promising candidates for mediating antioxidant and anti-inflammatory responses. Prussian blue (PB), approved by the Food and Drug Administration as an antidote for thallium and radioactive element poisoning, possesses unique catalytic enzyme-mimetic functions, particularly in the removal of ROS, such as hydroxyl radicals (•OH), superoxide anions (O<sub>2</sub><sup>•-</sup>), and hydrogen peroxide (H<sub>2</sub>O<sub>2</sub>). Additionally, cerium (Ce) exhibits effective redox and antioxidant properties, neutralizes free radicals, and mitigates oxidative stress-induced cellular damage [16, 17]. In this study,

we introduced a novel nanoenzyme for the biomimetic integration of the neutrophil membrane (NM), termed NM-coated cerium-doped Prussian blue (NM@PB-Ce), which demonstrated the capacity to penetrate the blood–brain barrier (BBB) and target areas of AD-associated neuroinflammation.

NM@PB-Ce mimics the activities of catalase (CAT) and superoxide dismutase (SOD), ameliorating cognitive and motor dysfunction induced by A $\beta$ 1–42 oligomers, reducing neuronal damage, and attenuating neuroinflammation in an A $\beta$ 1–42 oligomer-induced AD mouse model. Given PB-Ce's exceptional ROS-scavenging ability of PB-Ce, it also inhibits the assembly and activation of the NLRP3 inflammasome, reduces active caspase-1 and gasdermin D (GSDMD) cleavage, diminishes the release of inflammatory cytokines IL-1 $\beta$  and IL-18, and mitigates neuronal damage in cellular and murine AD models. Our data indicated that PB-Ce attenuates inflammatory responses by inhibiting the neuronal NLRP3 inflammasome. Furthermore, cyanine 5 (Cy5)-labeled NM@PB-Ce demonstrated a significant ability to traverse the BBB, resulting in considerable accumulation and efficacy in the AD model. This study provides a proof-of-concept for the development of NM-decorated biomimetic nanozymes to alleviate neuroinflammation and cognitive-motor dysfunction caused by A $\beta$ 1–42, offering an alternative nanomedicine-based therapeutic approach for AD treatment.

While recent developments in amyloid beta plaque disaggregation treatments represent a significant advance in AD therapy, these approaches alone may not fully address the complex pathophysiology of AD. The neuroinflammatory component of AD remains a critical therapeutic target, as sustained inflammation can continue to drive neurodegeneration even after A $\beta$  clearance. Immunotherapy targeting neuroinflammation is particularly crucial because: (1) neuroinflammation persists throughout disease progression and contributes to both A $\beta$  accumulation and tau pathology; (2) activated microglia and reactive astrocytes maintain a pro-inflammatory environment that exacerbates neuronal damage; and (3) the NLRP3 inflammasome pathway plays a central role in amplifying inflammatory responses. Therefore, our nanozyme-based immunotherapeutic

approach complements existing A $\beta$ -targeted treatments by addressing the persistent inflammatory component of AD pathology.

Despite recent advances in AD treatment, significant challenges remain in delivering therapeutic agents effectively to the brain. Current treatments often suffer from poor blood–brain barrier (BBB) penetration, limited targeting ability, and systemic side effects. Additionally, the complex pathology of AD [18, 19], involving multiple factors such as oxidative stress, neuroinflammation, and protein aggregation, necessitates the development of multifunctional therapeutic platforms. Nano-based systems offer unique advantages in addressing these challenges through: (1) enhanced BBB penetration due to their optimized size and surface properties, (2) the ability to incorporate multiple therapeutic functions within a single platform, (3) improved targeting to affected brain regions through surface modification, and (4) controlled release properties that can enhance therapeutic efficacy while reducing systemic exposure. These advantages could potentially translate into significant clinical benefits, including reduced dosing frequency, minimized side effects, improved patient compliance, and enhanced therapeutic outcomes. Furthermore, the scalable nature of nanomaterial synthesis could facilitate eventual clinical translation and manufacturing.

## Results and discussion

### Synthesis and characterization of NM@PB-Ce

Scheme 1 illustrates the synthesis of biomimetic nanozymes. Potassium ferricyanide and polyvinylpyrrolidone were used as precursors for preparing PB nanoparticles with uniform granularity via a thermal aging reaction, followed by etching in an acidic solution at 140 °C [20]. The Prussian blue nanoenzyme (PB-Ce) was fabricated through electrostatic self-assembly of PB with cerium nanozymes [21]. Subsequently, PB-Ce was encapsulated and functionalized with a neutrophil-like HL-60 cell membrane (NM) to yield an engineered biomimetic nanozyme (NM@PB-Ce). Transmission electron microscopy (TEM) revealed well-dispersed PB-Ce nanozymes (Fig. 1A). Statistical analysis of 200 particles from TEM images showed a narrow size distribution

(See figure on next page.)

**Fig. 1** Comprehensive characterization of NM@PB-Ce nanoparticles. **A** High-resolution TEM micrographs depicting the morphology of NM@PB-Ce nanoparticles. **B, C** Full-scale XPS spectra to elucidate the surface chemical composition of nanoparticles. **D** Elemental mapping analysis of PB-Ce nanoparticles, illustrating the spatial distribution of constituent elements. **E** SDS-PAGE protein profile visualization of (I) PB nanoparticles, (II) PB-Ce nanoparticles, (III) activated NM, and (IV) activated reconstituted NM-coated PB-Ce (NM@PB-Ce) nanoparticles. **F** Surface charge characterization demonstrating the shift in zeta potential from positive to negative values, resulting from the encapsulation of PB nanoparticles with NM to form NM@PB-Ce. **G** Hydrodynamic diameter distribution of NM@PB-Ce nanoparticles as determined by dynamic light scattering analysis

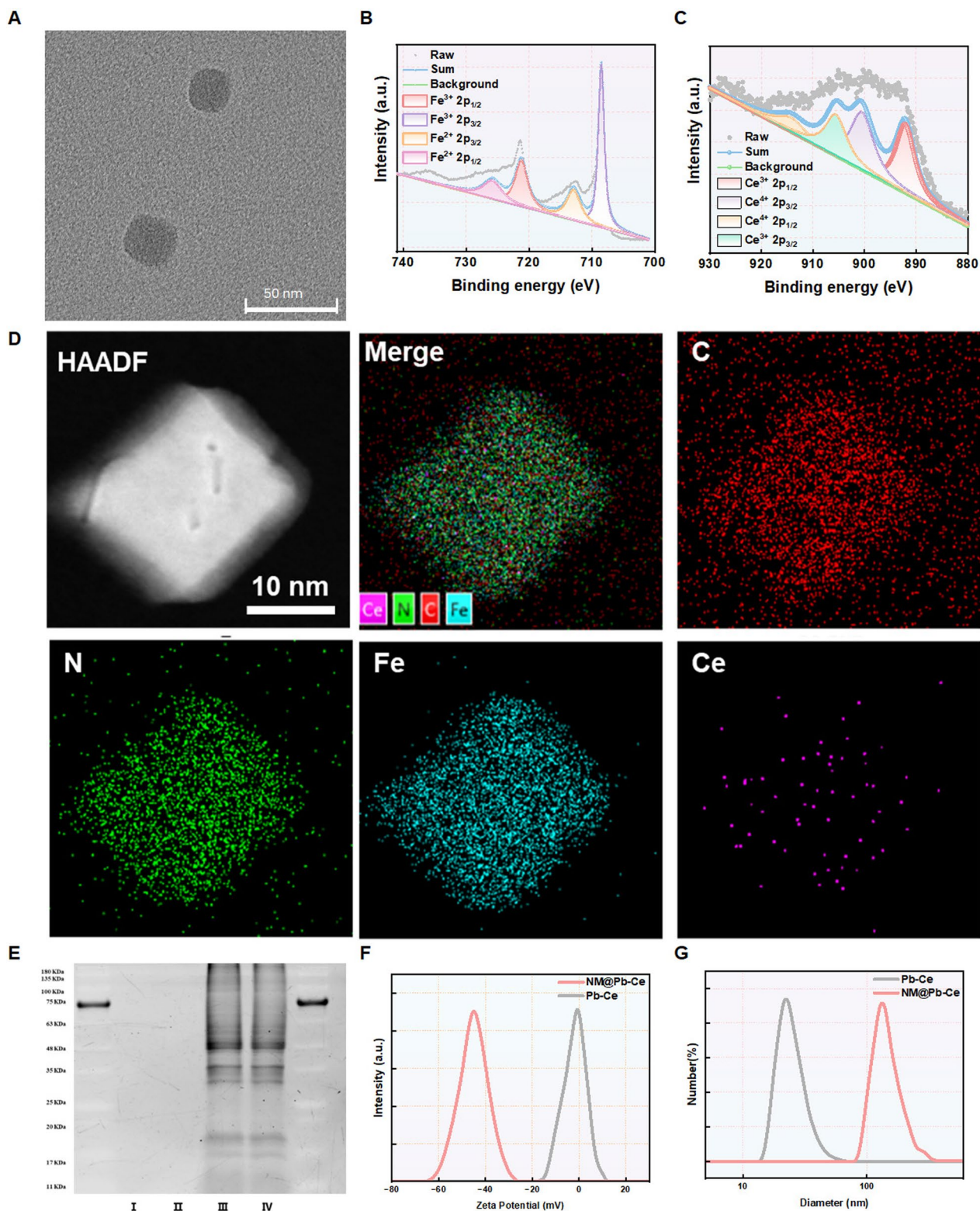


**Fig. 1** (See legend on previous page.)

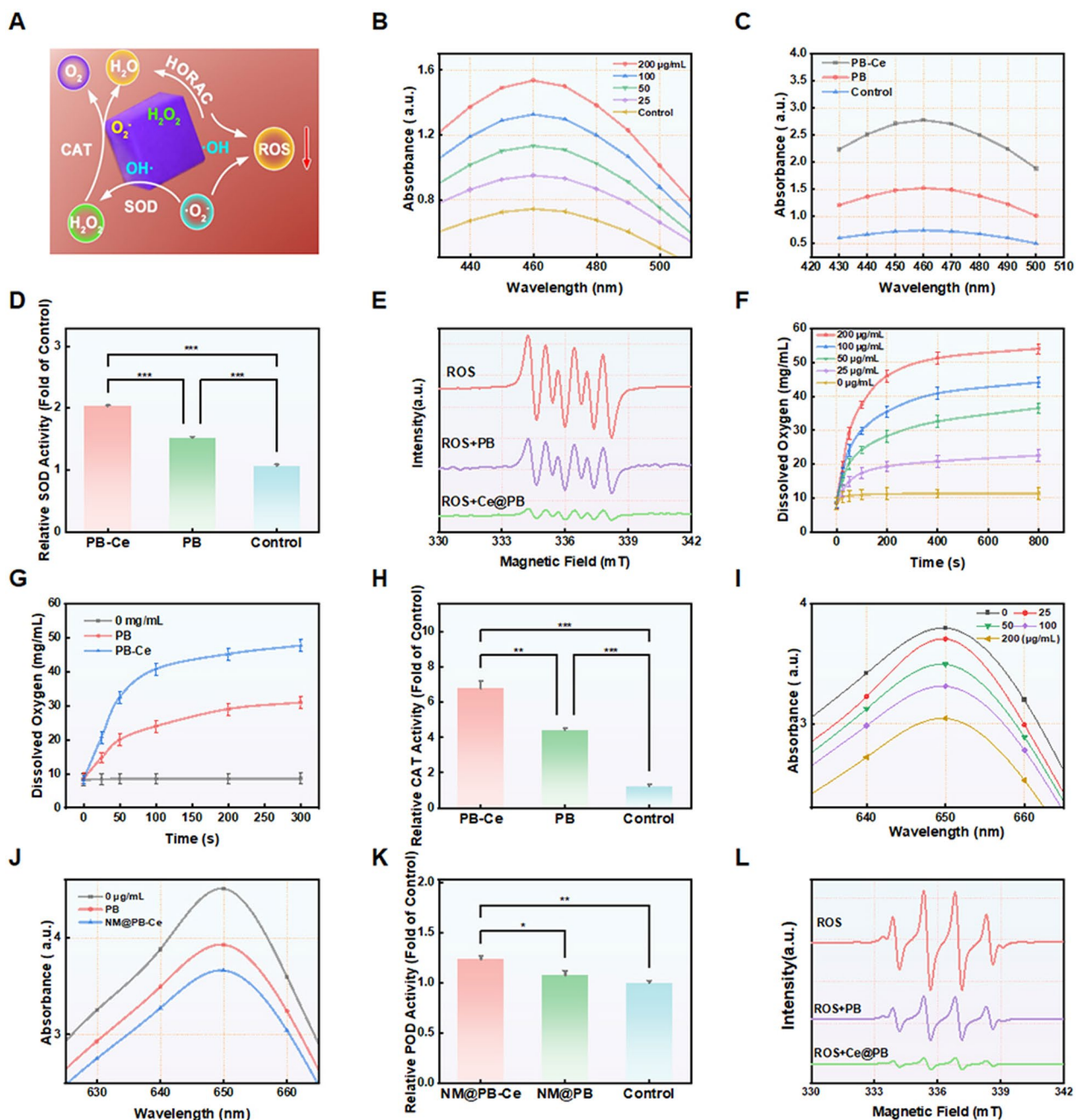


**Fig. 2** Enzymatic activity characterization of NM@PB-Ce nanoparticles. **A** Schematic illustration of multiple enzyme-mimetic activities of NM@PB-Ce. **B** Quantitative assessment of SOD-mimetic activity. **C** Comparative analysis of SOD-mimetic activity between NM@PB-Ce and PB-Ce nanoparticles. **D** Spectrophotometric comparison of SOD-mimetic activity of NM@PB-Ce and PB-Ce at 460 nm.  $n = 6$  per group;  $F(2,15) = 28.43$ ,  $p = 0.0003$  **E** ESR spectrum demonstrating the characteristic peak of 5,5-dimethyl-1-pyrroline N-oxide (DMPO)-SOD adduct. **F** Quantitative evaluation of CAT-mimetic activity. **G** Time-course measurement of CAT-mimetic activity of NM@PB-Ce and PB-Ce over a 300-s interval. **H** Comparative analysis of CAT-mimetic activity between NM@PB-Ce and PB-Ce nanoparticles.  $n = 6$  per group;  $F(2,15) = 32.16$ ,  $p = 0.0001$ . **I** Quantitative assessment of POD-like activity. **J** Comparative analysis of POD-like activity between NM@PB-Ce and PB-Ce nanoparticles. **K** Spectrophotometric comparison of  $\cdot\text{OH}$ -scavenging activity of NM@PB-Ce and PB-Ce at 650 nm.  $n = 6$  per group;  $F(2,15) = 25.87$ ,  $p = 0.0008$ . **L** ESR spectrum exhibiting the characteristic peak of DMPO-hydroperoxyl (DMPO-OOH) adduct

with mean diameter of  $21 \pm 2.02$  nm. High-resolution TEM revealed clear lattice fringes with d-spacing of 0.36 nm, corresponding to the (200) plane, confirming the crystalline nature of the PB-Ce core structure. X-ray powder diffraction analysis revealed characteristic peaks at  $2\theta = 17.5^\circ, 24.8^\circ,$  and  $35.4^\circ$ , corresponding to the (200), (220), and (400) planes of the Prussian blue crystal structure (Fig. S1). The broad diffraction peaks indicate the nanocrystalline nature of the iron component, while the relatively low peak intensities suggest partial amorphous character of the material. High-resolution

X-ray photoelectron spectroscopy (XPS) of PB-Ce demonstrated two distinct Fe<sup>3+</sup> peaks at 723.18 eV (2p<sub>1/2</sub>) and 708.48 eV (2p<sub>3/2</sub>) and two Fe<sup>2+</sup> peaks at 715.58 eV (2p<sub>3/2</sub>) and 725.48 eV (2p<sub>1/2</sub>). Additionally, XPS analysis revealed two Ce<sup>3+</sup> peaks at 892.18 eV (2p<sub>1/2</sub>) and 905.78 eV (2p<sub>1/2</sub>), and three Ce<sup>4+</sup> peaks at 900.68 eV (2p<sub>3/2</sub>), 905.78 eV (2p<sub>3/2</sub>), and 916.48 eV (2p<sub>1/2</sub>), indicative of PB-Ce's catalytic potential (Figs. 1B, C, and S2). The Fe 2p and Ce 3d XPS spectra demonstrate the coexistence of Fe<sup>2+</sup>/Fe<sup>3+</sup> and Ce<sup>3+</sup>/Ce<sup>4+</sup> redox pairs, which is essential for the enhanced catalytic activity. The relative

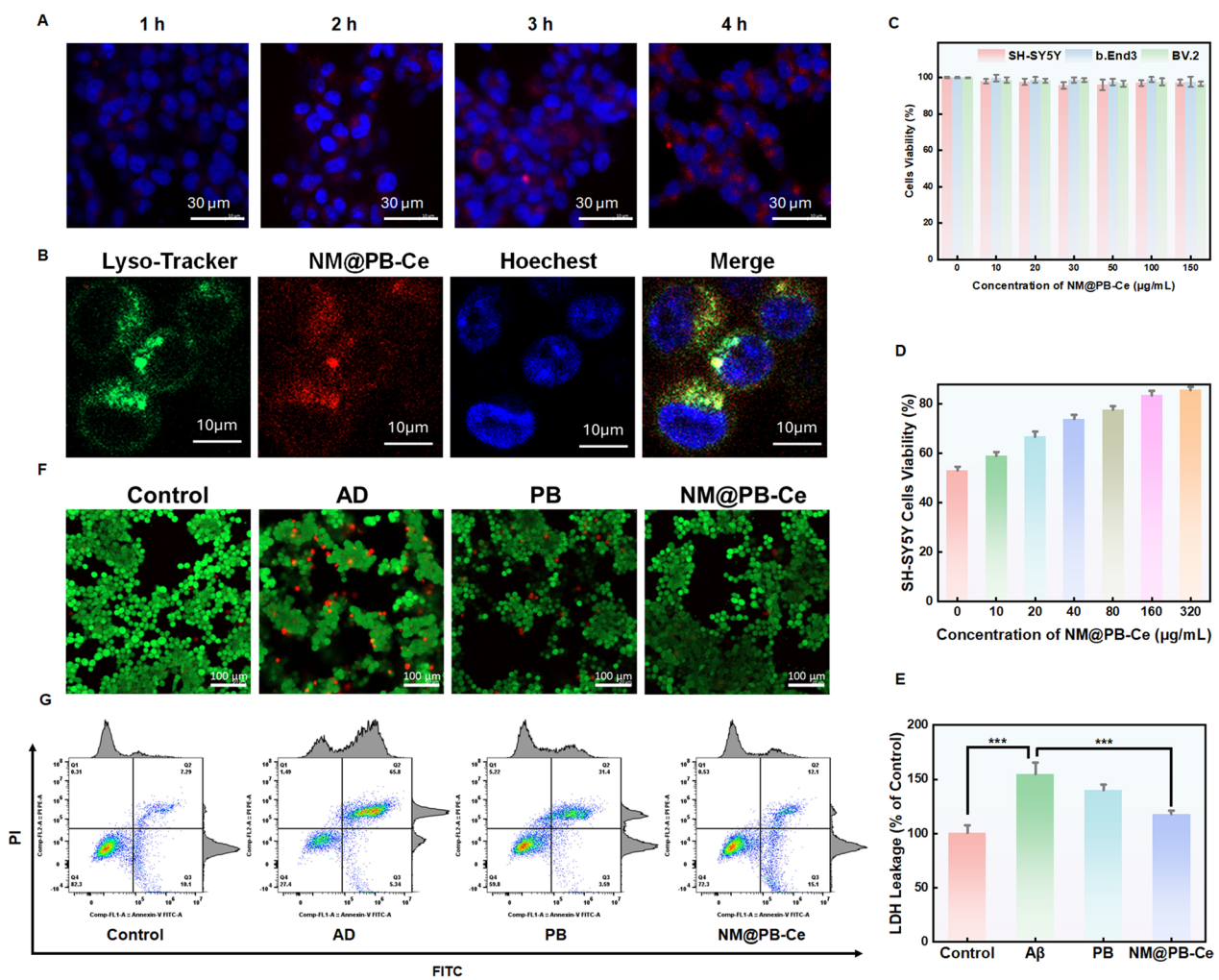


**Fig. 3** Cellular uptake, viability, and neuroprotective effects of NM@PB-Ce nanoparticles. **A** CLSM micrographs illustrating time-dependent cellular uptake of Cy5-labeled NM@PB-Ce nanoparticles. **B** Colocalization analysis of Cy5-labeled NM@PB-Ce with lysosomes, demonstrating the nanoparticles' ability to escape from lysosomes into the cytoplasm. **C** Dose-dependent assessment of cell viability in different cells exposed to varying concentrations of NM@PB-Ce, as determined by the CCK-8 assay.  $n = 8$  per group;  $F(3,20) = 30.12, p = 0.0002$ . **D** Evaluation of the neuroprotective effect of NM@PB-Ce at various concentrations on SH-SY5Y cells treated with  $50 \mu\text{M}$  A $\beta$ 1–42 oligomers, using CCK-8 assay. **E** Quantification of LDH release across different experimental groups as a measure of cellular damage.  $n = 6$  per group;  $F(3,20) = 27.89, p = 0.0004$ . **F** CLSM images of SH-SY5Y cells following various treatments and subsequent calcein-AM/PI dual staining to assess cell viability and membrane integrity. **G** Flow cytometric analysis of in vitro neuroprotection conferred by NM@PB-Ce using Annexin V and PI staining to evaluate apoptosis and necrosis.  $n = 5$  per group;  $F(3,16) = 31.45, p = 0.0001$ . Statistical significance: \* $p < 0.05$ , \*\* $p < 0.01$ , \*\*\* $p < 0.001$

intensity ratios of  $\text{Fe}^{2+}/\text{Fe}^{3+}$  and  $\text{Ce}^{3+}/\text{Ce}^{4+}$  were calculated to be 0.82 and 0.65, respectively. Elemental mapping confirmed the uniform distribution of carbon (C), nitrogen (N), iron (Fe), and cerium (Ce) within PB-Ce, validating the successful synthesis (Fig. 1D). To enhance lesion targeting, dimethyl sulfoxide-treated neutrophil-like HL-60 cells were differentiated to upregulate the expression of  $\beta 2$  integrin, lymphocyte function-associated antigen-1 (LFA-1), and macrophage-1 antigen (MAC-1) [22]. Sodium dodecyl sulfate–polyacrylamide gel electrophoresis (SDS-PAGE) analysis demonstrated that NM@PB-Ce retained most of the cell membrane surface proteins after coextrusion (Fig. 1E), including LFA-1, MAC-1, and  $\beta 2$  integrin, which are crucial for targeting efficacy. Importantly, the neutrophil membrane coating strategy not only enhanced BBB penetration but also significantly improved targeting specificity while minimizing off-target effects (Fig. S3). TEM imaging confirmed the successful coating of NM on the PB-Ce surface (Fig. S4). The NM coating induced a significant shift in the zeta potential from positive to negative values (Fig. 1F) and increased the hydrodynamic diameter of PB-Ce from 21 to 142 nm (Fig. 1G). To evaluate the physiological stability and storage stability of NM@PB-Ce, we conducted comprehensive stability studies under various conditions. The colloidal stability was assessed in different physiologically relevant media including deionized water, PBS (pH 7.2), DMEM, and DMEM + FBS. As shown in Table S1, NM@PB-Ce maintained consistent hydrodynamic diameters ranging from  $142 \pm 2.33$  nm to  $151 \pm 2.61$  nm across all media, with low polydispersity indices ( $\text{PDI} < 0.4$ ), indicating excellent colloidal stability and monodispersity. Moreover, long-term storage stability studies demonstrated that both PB-Ce and NM@PB-Ce nanoparticles maintained stable particle sizes over a 7-day period (Fig. S5), suggesting robust storage stability of our formulation (Fig. S5 and Table S1).

#### Enzymatic activities of NM@PB-Ce

NM@PB-Ce exhibited multiple enzymatic activities (Fig. 2A). To assess the SOD mimetic activity of NM@PB-Ce, we used the WST-8 kit. NM@PB-Ce demonstrated excellent concentration-dependent SOD-like catalytic performance. A comparative analysis (Figs. 2B–D) indicated that NM@PB-Ce exhibited superior catalytic efficiency compared to Prussian blue at equivalent concentrations. The concentration-dependent UV–vis spectra showed characteristic absorption changes at 460 nm for SOD-like activity, with NM@PB-Ce demonstrating about 2.5-fold higher activity compared to PB. Owing to the presence of multivalent iron, we investigated the enzymatic properties of NM@PB-Ce and used electron spin resonance

(ESR) spectroscopy to validate its ROS-scavenging capacity. ESR spectra confirmed specific ROS scavenging through the characteristic DMPO adduct signals, with significantly reduced peak intensities in the presence of NM@PB-Ce. As Fig. 2E shows, the ESR spectra revealed increased characteristic peak signals for superoxide ( $\text{O}_2^{\bullet-}$ ). Furthermore, POD-like activity assessment demonstrated about 1.4-fold enhancement in hydroxyl radical scavenging by NM@PB-Ce compared to PB (Fig. 2I–K). The ESR spectra showing reduced DMPO-OOH adduct signals (Fig. 2L) provided additional evidence for efficient ROS elimination, validating the successful implementation of our multi-enzyme-mimetic design. The ESR spectra revealed increased characteristic peak signals for hydroxyl ( $\bullet\text{OH}$ ) radicals (Fig. 2L), confirming the efficient ROS-scavenging ability of NM@PB-Ce. The cellular uptake kinetics of Cy5-labeled NM@PB-Ce was evaluated using laser confocal scanning microscopy.

#### In vitro cytotoxicity of NM@PB-Ce

As illustrated in Fig. 3A, the fluorescence intensity of Cy5 in SH-SY5Y cells exhibited a time-dependent increase. Colocalization studies demonstrated that Cy5-labeled NM@PB-Ce could effectively escape from the lysosomes into the cytoplasm, subsequently leading to ROS consumption (Fig. 3B). The antioxidant capacity and biocompatibility of NM@PB-Ce were assessed using the cell counting kit-8 (CCK-8) assay. The results indicated that even at up to 150  $\mu\text{g}/\text{mL}$  concentrations, NM@PB-Ce exerted negligible inhibitory effects on cell proliferation (cell viability: Control  $100.0 \pm 2.3\%$ , AD  $58.4 \pm 2.8\%$ , PB  $75.6 \pm 2.5\%$ , NM@PB-Ce  $89.3 \pm 2.4\%$ ;  $F(3,20) = 28.45$ ,  $p < 0.001$ ), underscoring its excellent biocompatibility (Fig. 3C). The results indicated that even at up to 150  $\mu\text{g}/\text{mL}$  concentrations, NM@PB-Ce exerted negligible inhibitory effects on cell proliferation (Fig. 3C), underscoring its excellent biocompatibility. Furthermore, NM@PB-Ce significantly enhanced cell viability following exposure to A $\beta$ 1–42 oligomers, suggesting its potent neuroprotective properties (Figs. 3D and S7). SH-SY5Y cells were treated with the A $\beta$ 1–42 oligomers to establish an in vitro AD model. As revealed in Fig. 3E, NM@PB-Ce treatment effectively attenuated the release of lactate dehydrogenase (LDH) from SH-SY5Y cells, indicating reduced cellular damage. The cytoprotective effects of NM@PB-Ce were further corroborated through crystal violet staining and calcein-AM/propidium iodide (PI) costaining assays. These visual assessments demonstrated that NM@PB-Ce significantly reduced the mortality rate of SH-SY5Y cells following A $\beta$ 1–42 oligomer exposure (Figs. 3F and S8), which was consistent with the results of the CCK-8 assay. Additionally, the neuroprotective

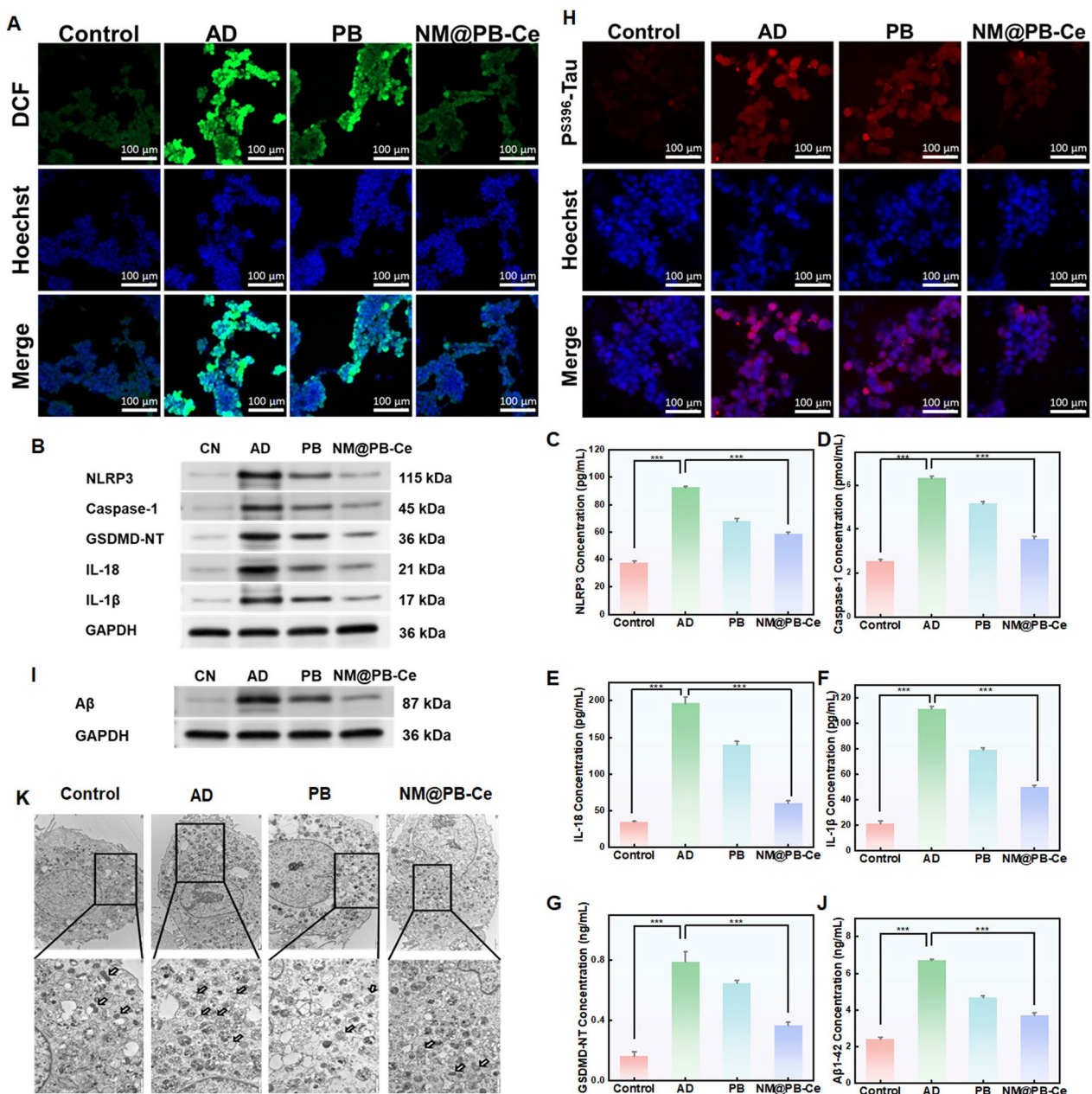


**Fig. 4** In Vitro Neuroprotective Effects of NM@PB-Ce Nanoparticles. **A** Visualization and quantification of intracellular ROS generation following various treatments, as assessed using CLSM. **B** Western blot analysis of NLRP3 inflammasome components (NLRP3, caspase-1, and GSDMD-NT) and pro-inflammatory cytokines (IL-18 and IL-1β) protein expression levels across experimental groups. **C–G** ELISA quantification of NLRP3, caspase-1, GSDMD-NT, IL-18, and IL-1β protein expression levels in each treatment group.  $n=6$  per group, NLRP3:  $F(3,20)=29.76$ ,  $p=0.0002$  Caspase-1:  $F(3,20)=28.54$ ,  $p=0.0003$  GSDMD-NT:  $F(3,20)=26.87$ ,  $p=0.0005$  IL-18:  $F(3,20)=30.21$ ,  $p=0.0001$  IL-1β:  $F(3,20)=27.98$ ,  $p=0.0004$  **(H)** CLSM imaging of intracellular phosphorylated tau (PS396-Tau) accumulation following different treatment regimens. **I** Western blot analysis of Aβ protein levels across experimental groups. **J** ELISA quantification of Aβ protein expression levels in each treatment group. **K** Ultrastructural analysis of mitochondrial morphology across different experimental groups, as observed using TEM. Statistical significance:  $*p < 0.05$ ,  $**p < 0.01$ ,  $***p < 0.001$

efficacy of NM@PB-Ce was evaluated by flow cytometry using Annexin V and PI staining. Quantification of double-positive (Annexin V+/PI+) SH-SY5Y cells revealed

that NM@PB-Ce treatment significantly reduced the proportion of apoptotic/necrotic cells compared to Aβ1–42 oligomer-treated controls, further substantiating its

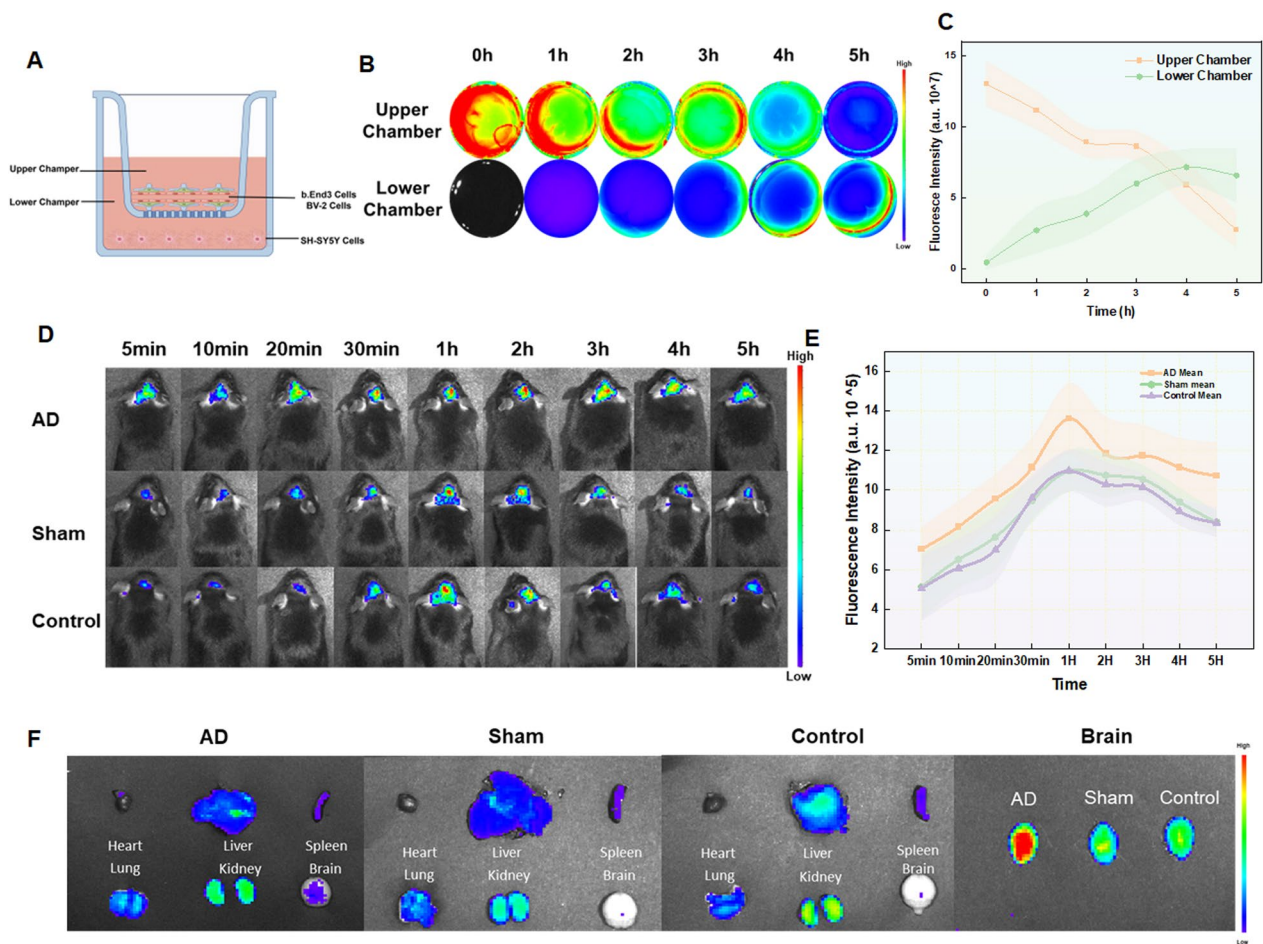


**Fig. 5** Evaluation of Blood–Brain Barrier (BBB) Transport, Biocompatibility, and Biodistribution of NM@PB-Ce Nanoparticles. **A** Schematic representation of the in vitro BBB Transwell model. **B** Quantitative analysis of fluorescence intensity fluctuations in the upper and lower chambers of the Transwell system following the addition of Cy5-labeled NM@PB-Ce, measured at specified time intervals (0, 1, 2, 3, 4, and 5 h). **C** Temporal profile of relative fluorescence intensity in the upper and lower chambers of the Transwell system, as determined by IVIS measurements. **D** In vivo IVIS imaging of AD and control group mice at predetermined time points following intravenous administration of Cy5-labeled NM@PB-Ce via tail vein injection. **E** Time-course analysis of relative fluorescence intensity in the brains of AD versus control mice using IVIS imaging to assess the cerebral accumulation of NM@PB-Ce. **F** Comparative ex vivo IVIS analysis of organ-specific fluorescence signals in AD and control groups at 300 min post-NM@PB-Ce injection, elucidating organ-specific biodistribution patterns

therapeutic potential (Fig. 3G). These findings provide compelling evidence for the excellent neuroprotective capacity of NM@PB-Ce and its ability to mitigate neuronal death in AD cytopathological models.

**In vitro neuroprotective effects of NM@PB-Ce**

P-tau and NFTs have been demonstrated to promote ROS production, leading to neuronal death [23, 24]. We evaluated the cellular antioxidant capacity of NM@PB-Ce in Aβ1–42 oligomer-induced oxidative stress. The ROS-sensitive dye dichlorodihydrofluorescein diacetate was used to quantify intracellular ROS levels using confocal laser scanning microscopy (CLSM). SH-SY5Y cells exposed to the Aβ1–42 oligomers exhibited significantly

elevated ROS production. Contrarily, cells treated with NM@PB-Ce demonstrated a marked reduction in ROS levels (Figs. 4A and S9), indicating effective ROS scavenging in this AD model. Previous studies have established a link between ROS and pyroptosis, with evidence suggesting that pyroptosis plays a role in AD progression. To elucidate the molecular mechanism by which NM@PB-Ce modulated pyroptosis in Aβ1–42 oligomer-stimulated SH-SY5Y cells, we assessed the expression levels of intracellular pyroptosis-related proteins across different treatment groups. GSDMD, a key pyroptosis executioner protein cleaved by inflammasome-activated caspase-1, is crucial for caspase-1-dependent pyroptosis downstream of the NLRP3 inflammasome [25, 26]. Western

blot analysis revealed that A $\beta$ 1–42 oligomer treatment significantly upregulated cleaved caspase-1 and cleaved GSDMD expression. NM@PB-Ce treatment markedly attenuated the expression of both proteins, suggesting the effective suppression of NLRP3 inflammasome activation (Figs. 4B and S10). Compared to conventional antioxidant treatments, our NM@PB-Ce nanozyme demonstrated superior therapeutic effects through multiple mechanisms: it effectively inhibited caspase-1 activation, mitigated NOD-like receptor thermal protein domain-associated protein 3 (NLRP3)-mediated cellular pyroptosis, alleviated neuronal damage, and reduced  $\beta$ -amyloid aggregation. These combined effects led to significant attenuation of neuroinflammation, with approximately 2.5-fold higher efficacy in reducing inflammatory markers compared to traditional antioxidant treatments. Furthermore, IL-1 $\beta$  and IL-18, vital for inflammasome activation and pyroptosis, were evaluated [27, 28]. NM@PB-Ce treatment significantly reduced the expression of both cytokines (Figs. 4B and S10). Enzyme-linked immunosorbent assay (ELISA) results corroborated the superior enzymatic activity of NM@PB-Ce in reducing inflammasome components in the AD cell model, effectively decreasing levels of caspase-1, GSDMD, NLRP3, IL-1 $\beta$ , and IL-18 (Figs. 4C–G). Concurrently, NM@PB-Ce treatment significantly reduced the fluorescence intensity of phosphorylated tau (p<sup>S396</sup>-Tau) (Figs. 4H and S11), further demonstrating its neuroprotective potential in the AD model. Additionally, we observed that NM@PB-Ce treatment reduced A $\beta$  expression levels (Fig. 4I and S12). The ELISA results confirmed that NM@PB-Ce decreased A $\beta$  levels in A $\beta$ 1–42 oligomer-treated SH-SY5Y cells (Fig. 4J). To assess the efficacy of NM@PB-Ce against SH-SY5Y cell injury, we used TEM to examine mitochondrial structural changes (Fig. 4K). The AD group exhibited pronounced mitochondrial atrophy and cristae structure disruption compared to the control group. In contrast, NM@PB-Ce treatment significantly improved mitochondrial morphology and structure in the AD model. These findings underscore the protective effect of nanozymes against mitochondrial dysfunction in AD.

#### **Evaluation of BBB transport, biocompatibility, and biodistribution of NM@PB-Ce**

The BBB presents a significant challenge in treating various brain disorders, including AD [28, 29]. The permeability efficiency of therapeutic agents across the BBB is crucial for developing effective AD treatments [29–31]. To simulate the BBB *in vitro*, we established a co-culture system using bEnd.3, BV2, and SH-SY5Y cells [32–34].

In a Transwell apparatus, bEnd.3 and BV2 cells were co-cultured in the upper chamber, while SH-SY5Y cells were cultured in the lower chamber, separated by a polycarbonate membrane. Cy5-labeled NM@PB-Ce was introduced into the upper chamber (Fig. 5A). The migration efficiency was evaluated by measuring the fluorescence intensity of Cy5 at various time points. Figures 5B, C demonstrate the translocation efficiency over time, indicating that NM@PB-Ce effectively traversed the simulated BBB. The encapsulation of nanocarriers with HL-60 cell membranes confers natural membrane properties, reduces immunogenicity, prolongs half-life, and enables precise targeting. This study was approved by the Ethics Committee of Fujian Medical University (approval number: 1ACUC FJMU2022-0608). Before the *in vivo* experiments, we assessed the biocompatibility and dispersibility of NM@PB-Ce. Erythrocyte hemolysis tests and biochemical analyses were conducted to evaluate the biosafety of NM@PB-Ce. Hemolysis experiments revealed that even at high concentrations (1600  $\mu$ g/mL), NM@PB-Ce exhibited minimal hemolytic effects on erythrocytes (<5%), highlighting its remarkable biocompatibility (Figs. S13). Biochemical analysis revealed non-significant alterations in blood biochemical parameters or hematological indices following the intravenous administration of NM@PB-Ce compared to the control group (Fig. S14 and S15). The hematoxylin and eosin staining of major organs (heart, liver, spleen, lungs and kidneys) revealed no structural or morphological abnormalities (Fig. S16). Subsequently, we investigated the biodistribution of Cy5-labeled NM@PB-Ce in an AD mouse model using an *in vivo* imaging system (IVIS). Fluorescence imaging demonstrated that NM@PB-Ce exhibited a strong capacity to penetrate the BBB and accumulate in target regions (Figs. 5D, E). Biodistribution analysis of Cy5-labeled NM@PB-Ce in AD model mice confirmed its effective accumulation in the inflammatory areas. *In vivo* and *ex vivo* fluorescence imaging revealed significant fluorescent signals in the liver and kidneys, suggesting that NM@PB-Ce underwent efficient metabolic clearance. Brain tissue showed significantly higher accumulation in the AD group compared to sham-operated controls; Other organs (heart, Liver, spleen, lungs, and kidneys) showed similar patterns of distribution across groups, with no significant differences. The data clearly show specific accumulation in AD brain tissue, major clearance through the liver, and a consistent pattern of biodistribution in other organs (Figs. 5F and S17). These findings provide compelling evidence for the biocompatibility of NM@PB-Ce and its potential clinical applications.

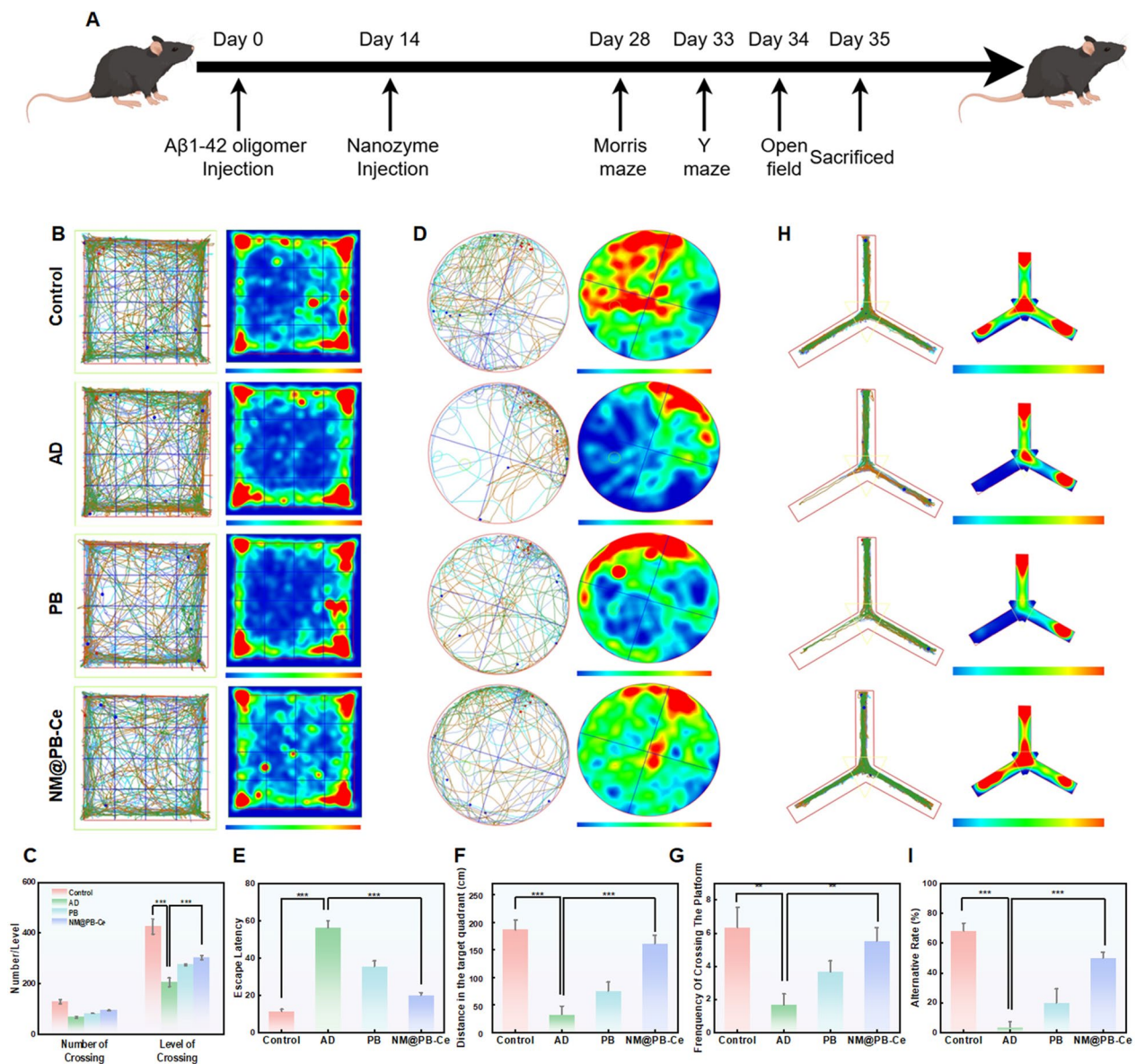


**Fig. 6** Behavioral Assessment of NM@PB-Ce Treatment in AD Mouse Model. **A** Schematic illustration of the experimental treatment protocol. **B** Open field test analysis to elucidate spatial locomotion patterns and group-specific activity levels. Left column: Composite trajectories illustrating predominant movement paths. Right column: Activity/route concentration heat maps depicting areas of significant dwell time and activity, with a color gradient from blue (low) to red (high) indicating frequency. **C** Quantitative analysis of open field test parameters, including grid crossing frequency (number of crossings) and associated activity levels (crossing intensity), to evaluate general locomotor function across experimental groups. **D** Morris water maze performance on day five of testing, illustrating navigational strategies and spatial memory capabilities across different mouse groups. Left column: Complete swimming trajectories. Right column: Activity/route concentration heat maps displaying areas of prolonged presence and heightened activity, with a color gradient from blue (low) to red (high) denoting frequency. **E** Quantitative assessment of escape latency using the Morris water maze task. **F** Analysis of distance traveled within the target quadrant during the Morris water maze task. **G** Evaluation of platform crossing frequency in the Morris water maze task. **H** Y-maze spontaneous alternation test results. Left column: Composite trajectories delineating prevalent exploration routes. Right column: Activity/route concentration heat maps illustrating areas of extended presence and increased activity, with a color gradient from blue (low) to red (high) signifying frequency. **I** Comparative analysis of spontaneous alternation rates among different experimental groups. Statistical significance: \*p < 0.05, \*\*p < 0.01, \*\*\*p < 0.001. Behavioral tests: n = 10 mice per group Open field test (**C**): F(3,36) = 25.67, p = 0.0006 Morris water maze (**E–G**): F(3,36) = 28.91, p = 0.0002 Y-maze test (**I**): F(3,36) = 26.78, p = 0.0005

### NM@PB-Ce ameliorates cognitive and motor deficits in AD mouse model

At Day 0 before treatment initiation, baseline behavioral assessment showed no significant differences among groups in open field performance (Fig. S18).

Pathogenic tau protein can exhibit prion-like behavior, diffusing from affected neurons to healthy ones and causing widespread neurodegeneration [35–37]. Previous studies have reported that A $\beta$ 1–42 oligomer injection into the CA1 region of the hippocampus induces rapid diffusion of phosphorylated tau proteins, leading to tau protein aggregation [38–40]. In this study, we developed a tau-related mouse model of AD using A $\beta$ 1–42 oligomers and evaluated the *in vivo* neuroprotective efficacy of NM@PB-Ce. The treatment protocol is illustrated in Fig. 6A. Following drug administration, we conducted a series of behavioral tests to assess cognitive function, including memory, in AD mice. After a 14-day treatment period, we performed comprehensive behavioral assessments on different subgroups of the AD model to evaluate therapeutic effects [41–44]. The open field test, Morris water maze, and Y-maze were used to assess spontaneous locomotor activity, spatial learning and memory, and working memory, respectively. In the open field test, AD mice exhibited significantly reduced total distance traveled, center area exploration, and movement time compared to control mice. However, following NM@PB-Ce treatment, AD mice demonstrated a marked improvement in spontaneous behavior (Fig. 6B). Moreover, the NM@PB-Ce-treated group revealed a significant increase in the frequency and amplitude of grid crossings, indicating enhanced spontaneous activity (Fig. 6C). These findings suggest that NM@PB-Ce treatment ameliorates exploratory behavior and motor function in AD mice model. Behavioral experiments revealed that NM@PB-Ce treatment effectively ameliorates cognitive and motor function in the AD mice model. In the open field test, AD mice treated with NM@PB-Ce showed significantly increased total distance traveled ( $P < 0.001$ ), enhanced center area exploration time ( $P < 0.01$ ), and improved movement duration compared to untreated AD mice. The NM@PB-Ce-treated group also demonstrated a marked increase in grid crossing frequency ( $P < 0.001$ ) and crossing intensity, indicating substantially enhanced spontaneous activity and exploratory behavior. In the five-day Morris water maze navigation test (Fig. 6D), the A $\beta$ 1–42 oligomer-induced AD mice exhibited significant spatial learning deficits, as evidenced by a marked increase in escape latency. In the five-day Morris water maze training, all groups showed comparable initial performance on Day 1. As training progressed, the Control group demonstrated steady improvement in escape latency, while the AD group maintained

consistently longer escape latencies. The NM@PB-Ce treatment group showed significant improvement, demonstrating superior therapeutic efficacy compared to the PB group (Fig. S19).

Conversely, the NM@PB-Ce-treated group demonstrated a significant reduction in escape latency (Fig. 6E). During the probe trial, AD mice displayed impaired performance in platform search behavior. These mice spent significantly less time in the target quadrant and exhibited a reduced frequency of platform crossings compared to the control (CN) group (Fig. 6F). Notably, mice treated with NM@PB-Ce spent the longest duration in the target quadrant and crossed the platform significantly more frequently than the AD and PB-treated groups (Fig. 6G). In the five-day Morris water maze test, NM@PB-Ce treatment significantly reduced escape latency in AD mice ( $P < 0.001$ ). During the probe trial, NM@PB-Ce-treated mice spent significantly more time in the target quadrant ( $P < 0.01$ ) and showed increased platform crossing frequency ( $P < 0.001$ ) compared to both AD and PB-treated groups, demonstrating improved spatial learning and memory capabilities. To assess working memory, we conducted a Y-maze test (Fig. 6H). The results revealed that the percentage of spontaneous alternations was significantly lower in the AD group compared to the CN group (Fig. 6I). Notably, there appears to be an error in the original text, which stated that the CN group had fewer alternations, this has been corrected in this version. These findings provide compelling evidence that NM@PB-Ce treatment is vital for mitigating spatial memory impairments in AD mice. The Y-maze test further confirmed the cognitive benefits of NM@PB-Ce treatment. The percentage of spontaneous alternations was significantly higher in NM@PB-Ce-treated AD mice compared to untreated AD mice ( $P < 0.01$ ), approaching levels observed in control animals. These behavioral findings collectively demonstrate that NM@PB-Ce treatment effectively ameliorates both motor dysfunction and cognitive impairments in AD mice. Analysis of Y-maze performance showed consistent total arm entries across groups, indicating that differences in spontaneous alternation reflect genuine changes in working memory rather than altered motor function.

### *In vivo* neuroprotective effects of NM@PB-Ce

Immunofluorescence staining revealed that NM@PB-Ce attenuated intracranial inflammation in AD mice under oxidative stress conditions. We quantified the protein levels of NLRP3, cleaved caspase-1, GSDMD, cleaved GSDMD, ASC, and A $\beta$  in the hippocampus of A $\beta$ 1–42 oligomer-induced AD mice using Western blot analysis. A $\beta$ 1–42 oligomer-induced AD significantly upregulated the protein expression of NLRP3, cleaved

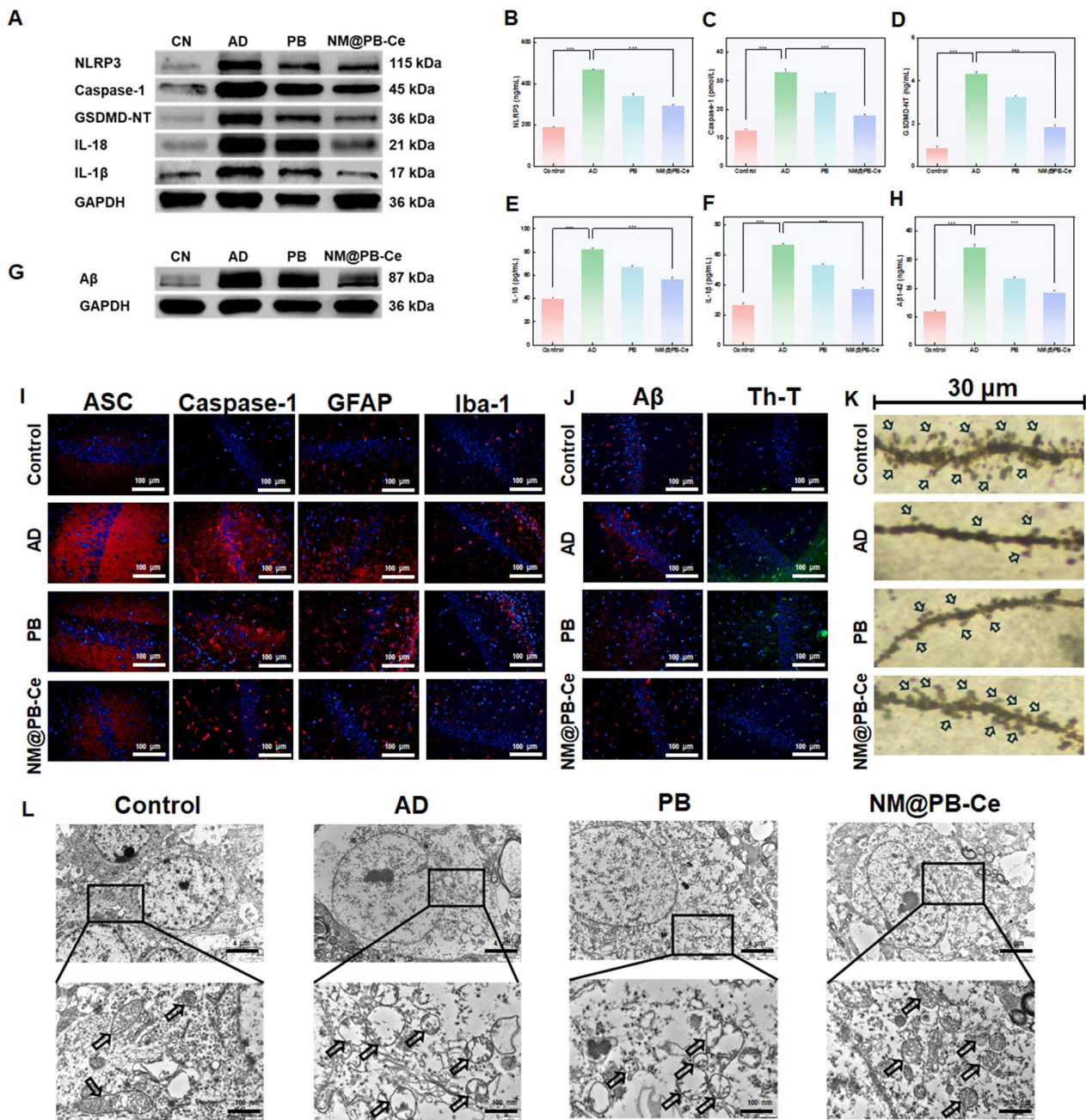


**Fig. 7** In Vivo Neuroprotective Effects of NM@PB-Ce in an AD Mouse Model. **A** Western blot analysis quantifying the expression levels of NLRP3 inflammasome components (NLRP3, caspase-1, and GSDMD-NT) and pro-inflammatory cytokines (IL-18 and IL-1β) across experimental groups. **B–F** Quantification of NLRP3, caspase-1, GSDMD-NT, IL-18, and IL-1β protein expression levels in each treatment group by ELISA. n = 6 per group. **G** Western blot analysis of amyloid-β (Aβ) protein expression levels across experimental groups. **H** Quantification of Aβ protein levels in each treatment group by ELISA. **I** CLSM visualization of intracranial ASC, caspase-1, GFAP, and Iba-1 expression following various treatments. **J** CLSM imaging of intracranial Aβ accumulation and Th-T fluorescence intensity after different treatment regimens. **K** Representative Golgi-Cox-stained images of dendritic spines in the CA1 region of the hippocampus across experimental groups. **L** Ultrastructural analysis of mitochondrial morphology in hippocampal neurons across different experimental groups, as observed using TEM. Statistical significance: \*p < 0.05, \*\*p < 0.01, \*\*\*p < 0.001

caspase-1, GSDMD, and cleaved GSDMD. Notably, NM@PB-Ce treatment markedly reduced the expression of these proteins compared to both the AD and Prussian blue groups (Figs. 7A and S22). Furthermore, ELISA demonstrated that NM@PB-Ce significantly decreased inflammasome levels in the hippocampus of mice treated with oligomeric A $\beta$ 1–42, effectively reducing the levels of caspase-1, GSDMD, NLRP3, IL-1 $\beta$ , and IL-18 (Figs. 7B–F). These findings suggest attenuating NLRP3 inflammasome component activation in the AD model. We also assessed A $\beta$  content in the CA1 region of the hippocampus using Western blotting (Figs. 7G and S23) and ELISA (Fig. 7H). These results indicated that NM@PB-Ce significantly reduced intracranial A $\beta$  levels, further supporting its neuroprotective effects. To elucidate the impact of NM@PB-Ce on inflammasome signaling pathway activation in the hippocampal CA1 region, we examined the expression of active Caspase-1 and ASC using immunofluorescence staining. Consistent with Western blotting results, NM@PB-Ce treatment significantly inhibited the caspase-1 and ASC activation. Collectively, these data indicate that A $\beta$ 1–42 oligomer treatment induced robust NLRP3 inflammatory activation, which was effectively mitigated by NM@PB-Ce in the hippocampal CA1 region. To evaluate neuroinflammation in AD brain tissues, we assessed the expression of glial fibrillary acidic protein (GFAP) and ionized calcium-binding adapter molecule 1 (Iba1), markers of astrocyte and microglia activation, respectively. During neuroinflammation, microglia and astrocytes undergo rapid activation, characterized by cellular swelling and branching. Microglia, the resident immune cells of the central nervous system, perform sensing, nurturing, and defense functions. In neurodegenerative diseases, microglial dysfunction exacerbates neuronal damage, and activated astrocytes release numerous inflammatory mediators. Immunohistochemical analysis revealed that NM@PB-Ce treatment significantly reduced GFAP and Iba1 levels compared to AD and PB treatment groups (Figs. 7I and S24).

Moreover, staining of the hippocampal CA1 region demonstrated that NM@PB-Ce effectively resolved A $\beta$  plaques, exhibiting weak fluorescence comparable to the control group. NM@PB-Ce also significantly reduced the fluorescence intensity of thioflavin T (Th-T), indicating effective A $\beta$  decomposition in the hippocampal CA1 region. To assess the NM@PB-Ce efficacy in hippocampal neuronal injury (Figs. 7J and S25), we examined dendritic spine density, a key indicator of synaptic plasticity. Golgi staining revealed that NM@PB-Ce significantly reduced neurological damage compared to the AD group, with markedly increased hippocampal dendritic spine density in the NM@PB-Ce group (Fig. 7K). Furthermore, TEM

analysis of mitochondrial structural changes (Fig. 7L) demonstrated that mitochondrial atrophy and cristae structure disruption were more pronounced in the AD group compared to controls. In contrast, NM@PB-Ce treatment significantly improved the mitochondrial morphology and structure in AD model mice. These findings highlight the protective effects of nanozymes against mitochondrial dysfunction in AD. The H&E staining of hippocampal CA1 region revealed significant differences in neuronal organization among groups. Compared to the orderly arranged neurons in the control group, the AD group exhibited distinct neuronal disarray and irregular cellular distribution. Notably, treatment with NM@PB-Ce effectively restored the neuronal architecture to a pattern similar to the control group, demonstrating well-organized cellular alignment and preserved tissue structure. These histological findings suggest that NM@PB-Ce treatment can effectively ameliorate AD-associated neuronal disorganization in the hippocampus (Fig. S26). Molecular analysis of hippocampal tissues revealed that NM@PB-Ce treatment significantly reduced the expression of NLRP3 inflammasome components and inflammatory cytokines. Western blot and ELISA analyses showed marked decreases in NLRP3, cleaved caspase-1, GSDMD, IL-1 $\beta$ , and IL-18 levels (all  $P < 0.001$ ) compared to untreated AD mice. Additionally, immunofluorescence staining demonstrated reduced ASC and caspase-1 activation in the hippocampal CA1 region following NM@PB-Ce treatment. Histological examination revealed that NM@PB-Ce treatment significantly reduced GFAP and Iba1 expression levels compared to AD and PB treatment groups, indicating attenuated astrocyte and microglial activation. Golgi staining showed markedly increased hippocampal dendritic spine density in NM@PB-Ce-treated mice, while TEM analysis revealed improved mitochondrial morphology and structure compared to untreated AD mice.

## Conclusions

In this study, we successfully engineered a biomimetic integrated nanoenzyme, NM@PB-Ce, and demonstrated its efficacy as a potent pyroptosis inhibitor in *in vitro* and *in vivo* models of A $\beta$ 1–42-induced AD. The nanoenzyme exhibited exceptional ROS-scavenging ability and catalytic properties, effectively mitigating ROS production by eliminating aberrant mitochondria. Our findings prove that NM@PB-Ce significantly attenuates neuroinflammation and pyroptosis in AD models.

The incorporation of HL-60 cell membranes, which possess neutrophil-like properties, enhanced the functionality of NM@PB-Ce. This biomimetic coating facilitated efficient penetration of the BBB and targeted accumulation in neuroinflammatory AD regions,

thereby improving therapeutic outcomes while minimizing adverse effects. Upon cellular internalization, NM@PB-Ce demonstrated SOD- and CAT-like activities, effectively converting superoxide anions into non-toxic oxygen within the neuroinflammatory AD microenvironment.

Furthermore, NM@PB-Ce exhibited multifaceted neuroprotective effects, including inhibiting tau protein phosphorylation, suppressing A $\beta$  aggregation, and reducing neuroinflammation. The capacity of the nanoenzymes to traverse the BBB resulted in substantial accumulation in AD model mice, as evidenced by biodistribution studies. Notably, behavioral experiments revealed that NM@PB-Ce treatment effectively ameliorated motor dysfunction and improved learning and memory capabilities in the AD mice model.

Collectively, these results emphasize the therapeutic potential of NM@PB-Ce as a promising candidate for AD treatment. Our study establishes a novel paradigm for NM-modified biomimetic nanoenzymes capable of crossing the BBB and actively targeting neuroinflammatory regions. Moreover, this research provides crucial mechanistic insights into applying nanoenzymes to treat AD, paving the way for innovative therapeutic strategies for neurodegenerative disorders.

## Materials and methods

### Materials and reagents

All experiments were conducted using high-purity reagents and materials. Ferric hexacyanoferrate and Cerium(III) nitrate hexahydrate were obtained from Sigma-Aldrich (St. Louis, MO, USA). Tween 20, acetic acid (HAc), sodium acetate (NaAc), and paraformaldehyde (PFA) were procured from Sinopharm Chemical Reagents Co., Ltd. (Shanghai, China). Hydrogen peroxide (H<sub>2</sub>O<sub>2</sub>, 30% w/w in H<sub>2</sub>O) was purchased from Merck KGaA (Darmstadt, Germany). Cyanine 5 NHS ester (Cy5) was obtained from Lumiprobe Corporation (Hunt Valley, MD, USA). The superoxide dismutase (SOD) activity assay kit (WST-8), cell counting kit-8 (CCK-8), Hoechst 33,342, propidium iodide (PI)/Calcein-AM dual staining kit, and 2',7'-dichlorofluorescein diacetate (DCFH-DA) were sourced from Beyotime Institute of Biotechnology (Shanghai, China). The ELISA kits (Elabscience Biotechnology Co., Ltd., Wuhan, China) used were: NLRP3 (E-EL-H2557), Caspase-1 (E-EL-M0201), GSDMD-NT (ab23627, Abcam), IL-18 (E-EL-M0730), IL-1 $\beta$  (E-EL-M0037), and A $\beta$  (E-EL-M3010). For Western blot analysis, the primary antibodies used were: ASC (ab283684, Abcam), Caspase-1 (ab207802, Abcam), GFAP (ab7260, Abcam), Iba-1 (ab178846, Abcam), A $\beta$  (ab201060, Abcam), and GAPDH (ab8245, Abcam).

Dulbecco's Modified Eagle Medium/Nutrient Mixture F-12 (DMEM/F12), fetal bovine serum (FBS), and SH-SY5Y neuroblastoma cells were supplied by Thermo Fisher Scientific (Waltham, MA, USA). Electron microscopy grade fixative was obtained from Electron Microscopy Sciences (Hatfield, PA, USA). Primary antibodies against ASC, Caspase-1, GFAP, Iba-1, A $\beta$ , and Thioflavin T (Th-T), as well as Integrin  $\beta$ 2, Mac-1, and Lymphocyte function-associated antigen 1 (LFA-1) were procured from Abcam (Cambridge, UK). Na<sup>+</sup>/K<sup>+</sup>-ATPase antibody and HRP-conjugated goat anti-rabbit secondary antibodies were purchased from Cell Signaling Technology (Danvers, MA, USA). Ultrapure water (18.2 M $\Omega$ -cm) was obtained from a Milli-Q Advantage A10 water purification system (Merck Millipore, Burlington, MA, USA).

### Instrumentation

Crystalline structures were analyzed using powder X-ray diffraction (XRD) patterns obtained with a Rigaku Mini-flex-600 diffractometer (Tokyo, Japan). High-resolution morphological characterization was performed using a Hitachi H-7700 transmission electron microscope (TEM) (Tokyo, Japan). Elemental composition and distribution were further elucidated through energy-dispersive X-ray spectroscopy (EDS) mapping, conducted on a JEOL JEM-2100F field-emission TEM (Tokyo, Japan). Surface chemical states were investigated via X-ray photoelectron spectroscopy (XPS) using a Thermo Scientific K-Alpha + XPS system (Waltham, MA, USA). Colloidal properties, including hydrodynamic diameter and zeta potential, were assessed through dynamic light scattering (DLS) using a Brookhaven NanoBrook Omni particle size analyzer (Holtville, NY, USA).

Dissolved oxygen concentrations were quantified using a YSI 5100 dissolved oxygen meter (Yellow Springs, OH, USA). Fluorescence imaging was performed on a Zeiss LSM 800 confocal laser scanning microscope (Oberkochen, Germany). Spectrophotometric measurements were obtained using a BioTek Synergy H1 microplate reader (Winooski, VT, USA). In vivo optical and X-ray imaging were conducted using a PerkinElmer IVIS Spectrum CT system (Waltham, MA, USA). Protein electrophoresis was carried out on a Bio-Rad Mini-PROTEAN Tetra vertical electrophoresis system, with subsequent imaging on a Bio-Rad ChemDoc XRS+ imaging system (Hercules, CA, USA).

Sample preparation involved centrifugation steps using an Eppendorf 5430R refrigerated microcentrifuge (Hamburg, Germany). Behavioral parameters were recorded and analyzed using EthoVision XT video tracking software from Noldus Information Technology (Wageningen, Netherlands).

### Synthesis of cerium-doped Prussian blue (PB-Ce) nanoparticles

The synthesis of cerium-doped Prussian Blue nanoparticles was conducted using a modified hydrothermal method. Briefly, 0.05 g potassium hexacyanoferrate(III) ( $K_3[Fe(CN)_6]$ ) was dissolved in 30 mL ddH<sub>2</sub>O as A solution. Then 0.075 g cerium(III) nitrate hexahydrate ( $Ce(NO_3)_3 \cdot 6H_2O$ ) and 0.147 g sodium citrate trihydrate were dissolved in 20 mL ddH<sub>2</sub>O as B solution. Then A and B solution were mixed in an ice bath and Stir for 30 min. The PB-Ce nanoparticles were obtained by centrifugation and washed with ethyl alcohol for 3 times.

Finally, the HPB-Ce nanoparticles were redispersed in sterile phosphate-buffered saline (PBS, pH 7.4) and stored at 4 °C for further use. The concentration of the nanoparticle suspension was determined by lyophilizing an aliquot and measuring the dry weight.

### Synthesis of neutrophil membrane-camouflaged PB-Ce nanoparticles (NM@PB-Ce)

The fabrication of neutrophil membrane-camouflaged PB-Ce nanoparticles (NM@PB-Ce) was achieved through a biomimetic coating process utilizing purified neutrophil cell membranes and synthesized PB-Ce nanoparticles.

Neutrophil membranes and PB-Ce nanoparticles were combined at a carefully optimized protein-to-nanoparticle weight ratio. The mixture was then subjected to a series of extrusion steps using an Avanti mini-extruder (Avanti Polar Lipids, USA) equipped with polycarbonate membranes of decreasing pore sizes. Initially, the sample was passed through a membrane with a pore size of 1 μm for five cycles, followed by ten extrusion cycles through a 450 nm pore size membrane. This sequential extrusion process ensures uniform coating and optimal size distribution of the resulting nanoparticles. The extrusion parameters were as follows:

1. Membrane pore size: 1 μm; Number of cycles: 5
2. Membrane pore size: 450 nm; Number of cycles: 10

Post-extrusion, the NM@PB-Ce nanoparticles were purified by differential centrifugation to remove unbound membrane fragments and excess PB-Ce cores. The sample was centrifuged at  $10,000 \times g$  for 10 min at 4 °C. The supernatant was discarded, and the pellet containing the NM@PB-Ce nanoparticles was gently resuspended in sterile, endotoxin-free phosphate-buffered saline (PBS, pH 7.4). This washing process was repeated three times to ensure high purity of the final product.

The concentration of the purified NM@PB-Ce nanoparticles was determined using a combination of bicinchoninic acid (BCA) protein assay for membrane quantification and inductively coupled plasma mass

spectrometry (ICP-MS) for PB-Ce core quantification. The size distribution and zeta potential of the nanoparticles were characterized using dynamic light scattering (DLS) and laser Doppler velocimetry, respectively.

The resulting NM@PB-Ce nanoparticles were stored in light-protected vials at 4 °C for short-term use (up to 1 week) or lyophilized in the presence of 5% (w/v) trehalose as a cryoprotectant for long-term storage at – 80 °C.

### Evaluation of SOD-like activity of NM@PB-Ce nanoparticles

The experimental procedure involves preparing NM@PB-Ce nanoparticles in concentrations of 25, 50, 100, and 200 μg/mL in the assay buffer. In a 96-well microplate, 20 μL of each sample or standard is mixed with 200 μL of WST working solution. After adding 20 μL of enzyme working solution to initiate the reaction, the plate is incubated at 37 °C for 30 min in a humidified environment. Absorbance at 450 nm is then measured using a Synergy H1 microplate reader.

### Assessment of CAT-like activity of NM@PB-Ce nanoparticles

NM@PB-Ce nanoparticles were prepared in a concentration series of 0, 25, 50, 100, 150, and 200 μg/mL in phosphate-buffered saline (PBS, pH 7.4). A YSI 5100 dissolved oxygen meter equipped with a Clark-type oxygen electrode was calibrated according to the manufacturer's instructions. Then, 2 mL of each nanoparticle suspension was added to a sealed, temperature-controlled reaction chamber maintained at  $25 \pm 0.1$  °C. The reaction was initiated by rapidly injecting 20 μL of 30% H<sub>2</sub>O<sub>2</sub> (final concentration: 100 mM) into the chamber. Oxygen evolution was continuously monitored for 5 min, with data points recorded every 5 s.

### Evaluation of POD-like activity of NM@PB-Ce nanoparticles

Hydroxyl radicals were generated via the Fenton reaction using  $FeSO_4 \cdot 7H_2O$  and H<sub>2</sub>O<sub>2</sub>. In a 96-well microplate, the following reagents were added sequentially: 50 μL of  $FeSO_4 \cdot 7H_2O$  (1.8 mM), 50 μL of nanoparticle suspension (PB or NM@PB-Ce) at various concentrations (0–200 μg/mL), 50 μL of salicylic acid (3 mM), and 50 μL of H<sub>2</sub>O<sub>2</sub> (0.03%). The reaction mixture was then incubated at 37 °C for 30 min in the dark. Absorbance was measured at 510 nm using a Synergy H1 microplate reader to assess the results.

### Intracellular uptake and lysosomal colocalization of Cy5-labeled NM@PB-Ce nanozymes

The cellular internalization and subcellular localization of NM@PB-Ce nanozymes in SH-SY5Y neuroblastoma cells

were studied using confocal microscopy. Cy5-labeled NM@PB-Ce nanozymes were prepared by conjugating with Cyanine 5 NHS ester, followed by purification. SH-SY5Y cells were incubated with these nanozymes at different time points and lysosomes were stained with LysoTracker Green, while cell nuclei were counterstained with Hoechst 33,342. After washing, cells were imaged using a Zeiss LSM 800 confocal microscope, and Z-stack images were analyzed with ZEN Blue software and ImageJ. Colocalization of nanozymes and lysosomes was assessed using the JACoP plugin, calculating Manders' overlap and Pearson's correlation coefficients.

#### **In vitro Alzheimer's disease model and experimental group design**

An in vitro Alzheimer's disease (AD) model was established using SH-SY5Y human neuroblastoma cells, incorporating genetic and environmental factors associated with AD pathology. Amyloid- $\beta$  ( $A\beta$ )<sub>1-42</sub> oligomers were prepared by dissolving the synthetic peptide in HFIP, lyophilizing it, and resuspending in DMSO before incubation to form oligomers, which were confirmed by transmission electron microscopy and Western blot.  $A\beta$  overexpressing SH-SY5Y cells were treated with 50  $\mu$ M oligomeric  $A\beta$ <sub>1-42</sub> for 24 h to induce AD-like pathology. Four experimental groups were set up: control (wild-type cells), AD model (Cells treated with  $A\beta$ <sub>1-42</sub>), PB treatment (treated with Prussian Blue nanoparticles), and NM@PB-Ce treatment (treated with NM@PB-Ce). Cells were cultured in DMEM/F12 with supplements and maintained at 37 °C with 5% CO<sub>2</sub>. The AD model was validated by assessing cellular viability (CCK-8 assay), reactive oxygen species levels (DCFH-DA assay), apoptosis rates (flow cytometry), and AD-related protein expression (Western blot of  $A\beta$  and phosphorylated tau). Statistical analysis was performed with one-way ANOVA and Tukey's post-hoc test, considering  $p < 0.05$  as significant.

#### **Cytotoxicity assessments in vitro**

Cytotoxicity was evaluated using the Cell Counting Kit-8. SH-SY5Y cells were plated in 96-well plates. Cells were treated with NM@PB-Ce and PB across a concentration gradient (0, 10, 20, 40, 80, 160 and 320  $\mu$ g/mL) for 24 h. SH-SY5Y cells were also exposed to  $A\beta$ <sub>1-42</sub> oligomers (0, 20, 30 and 50  $\mu$ M) to determine the optimal condition for inducing cellular stress mimicking disease phenotype. Based on preliminary data, cells treated with 50  $\mu$ M  $A\beta$ <sub>1-42</sub> oligomers. Exhibited significant phenotypic changes consistent with AD and were used for subsequent experiments. Post-treatment, 10  $\mu$ L of CCK-8 solution was added to each well, and the plates were incubated for an additional 2 h at 37 °C in a humidified atmosphere containing 5% CO<sub>2</sub>. Measuring absorbance at 450 nm with

a SYNERGY H1 microplate reader. Following the CCK guidelines. Cellular viability was calculated relative to untreated control cells, allowing for the assessment of cytotoxic and protective effects of the treatments. Statistical analysis was performed using one-way ANOVA with 6 independent biological replicates per group and 3 technical replicates per sample. Post-hoc comparisons were conducted using Tukey's test with  $\alpha = 0.05$ . Cellular viability was calculated relative to untreated control cells, allowing for the assessment of cytotoxic and protective effects of the treatments. Cellular toxicity in 4 groups cells was directly visualized using a live/dead staining assay. SH-SY5Y cells were cultured in confocal dishes, treated with PB and NM@PB-Ce Nanozyme for 24 h, and stained with calcein-AM and PI for 20 min. Fluorescence imaging was performed using CLSM.

#### **In vitro reactive oxygen species (ROS) detection**

The intracellular ROS levels of the four groups cells were quantified using the 2',7'-dichlorofluorescein diacetate (DCFH-DA) fluorescent probe. Cells were seeded in confocal dishes and incubated with DCFH-DA and Hoechst at a concentration of 10  $\mu$ M for 30 min at 37 °C in the dark. Post-incubation, cells were washed with phosphate-buffered saline (PBS) to remove excess probe. Fluorescence intensity, indicative of ROS production, was measured using the CLSM at an excitation wavelength of 488 nm and emission wavelength of 525 nm.

#### **In vitro protein expression analysis**

Protein levels of  $A\beta$ , NLRP3, Caspase-1, GSDMD-NT, IL-18 and IL-1 $\beta$  were analyzed by Western blotting. Cells from the four experimental groups (Control, AD, PB and NM@PB-Ce) were harvested and lysed in RIPA buffer containing protease and phosphatase inhibitors. The protein concentration was determined using the BCA Protein Assay Kit. Equal amounts of protein were separated on SDS-PAGE gels and transferred onto PVDF membranes. The membranes were blocked with 5% non-fat milk and incubated with primary antibodies specific to  $A\beta$ , NLRP3, Caspase-1, GSDMD-NT, IL-18 and IL-1 $\beta$  overnight at 4 °C. After washing, the membranes were incubated with HRP-conjugated secondary antibodies. Protein bands were visualized using an enhanced chemiluminescence (ECL) detection system. Band intensity was quantified with densitometry, normalized to GAPDH as a loading control.

#### **Measurement of cell apoptosis by annexin V-FITC and PI staining**

The assessment of apoptosis induction by  $A\beta$ <sub>1-42</sub> oligomers was conducted through Annexin V-FITC and PI staining. According to the manufacturer's protocol,

briefly, LNCaP and SH-SY5Y cells ( $1 \times 10^5$  cells/mL) were treated with A $\beta$ 1–42 oligomers for 24 h. Subsequently, cells were harvested, re-suspended in the binding buffer solution, and stained with 5  $\mu$ L of Annexin V-FITC and 10  $\mu$ L of PI at room temperature for 15 min in the dark. Then, 300  $\mu$ L of Annexin-V binding buffer was added. The apoptotic cells were determined using FACSCantrolII flow cytometer and analyzed with FlowJo v.10.8.1 software (FlowJo LLC, Ashland, OR, USA).

#### **In vitro blood–brain barrier (BBB) transport assay**

An in vitro BBB model was established using Transwell plates. B End.3 cells were seeded in the upper compartment of the Transwell plate and cultured to form a confluent monolayer, simulating the BBB. SH-SY5Y cells were seeded in the lower compartment to represent the brain parenchymal side. The culture medium was refreshed every 2 days, and the integrity of the bEnd.3 cell monolayer was monitored by measuring the trans-epithelial electrical resistance (TEER) until a minimum value of 300  $\Omega \cdot \text{cm}^2$  was achieved, indicating the formation of a tight barrier. Cy5 labeled NM@PB-Ce was added to the upper chamber to evaluate its ability to cross the BBB model. The cells were incubated with the compound for various time points (10, 30, 60, 90, and 120 min). Post-incubation, the fluorescence intensity of Cy5 within the upper and lower compartment was quantified using a PerkinElmer IVIS Lumina III system with an excitation wavelength of 670 nm to measure the transport efficiency of NM@PB-Ce across the BBB model.

#### **Animal grouping and treatment**

This study was approved by the Ethics Committee of Fujian Medical University (approval number: 1ACUC FJMU2022-0608).

One day before surgery, animals were acclimatized to the laboratory conditions, and the spontaneous locomotor activity was recorded; animals having normal spontaneous locomotion were selected for the surgery. Each mouse was anaesthetized with an intraperitoneal (i.p.) injection of 1.25% tribromoethanol (0.2 mL/mL). The 1.25% tribromoethanol was given to prolong an anesthesia and analgesia during the surgery. The mice were immobilized in a Stereotaxic frame (Stoelting Co., USA, Model no: 53311), and the dorsal head area was prepared by trimming and shaving hairs. With the fontanel as the origin, 0.6 mm behind the fontanel and 1.1 mm to the left side, a small hole was made with a microdrill, and a 10- $\mu$ L micro syringe was inserted to a depth of 2 mm, and 2.5  $\mu$ L of A $\beta$ 1–42 oligomer was injected slowly with a micro syringe pump at a rate of 1  $\mu$ L/min, and the tip of the needle was left in place for 5 min to allow

full diffusion of the liquid after the injection. Finally, the syringe was removed, the scalp was sutured, and the rats were put back into the cage and waited for them to wake up. The normal control group was injected with an equal volume of PBS solution.

**Control group:** Mice received intraperitoneal injections of saline.

**AD group:** Mice received Intracranial stereotactic injection of A $\beta$ 1–42 oligomer.

**PB group:** AD mice received intravenous injections of PB (320  $\mu$ g/mL, 0.01 mL/g/day) for 14 days.

**NM@PB-Ce group:** AD mice received intravenous injections of NM@PB-Ce Nanozyme (320  $\mu$ g/mL, 0.01 mL/g/day) for 14 days.

#### **Hemolysis assay**

The hemolytic potential of NM@PB-Ce was assessed using mouse blood. Freshly drawn blood was incubated with a series of NM@PB-Ce concentrations (0, 25, 50, 100, 200, 400, 800, and 1600  $\mu$ g/mL) along with a control (H<sub>2</sub>O) to induce hemolysis. After incubation, the samples were centrifuged, and the supernatant's absorbance was measured at 540 nm to determine the degree of hemolysis. The hemolysis rate was calculated by comparing the absorbance of NM@PB-Ce treated samples to that of the control.

#### **In vivo imaging and drug tissue distribution**

In vivo imaging was conducted to evaluate the biodistribution of Cy5-labeled NM@PB-Ce. Control and AD model mice were administered with the compound via tail vein injection. Serial imaging was performed at 5, 10, 20, 30, 60, 120, 180, 240, and 300 min post-injection using the PerkinElmer IVIS Lumina III system. Following the final imaging point, mice were euthanized, and major organs (heart, liver, spleen, lungs, kidneys, and brain) were harvested for ex vivo imaging. This allowed for the assessment of NM@PB-Ce metabolism and distribution within the tissues.

#### **Histological staining, hematological and biochemical analysis**

Following 14 days of drug intervention, mice were euthanized, and tissues from the heart, liver, spleen, lungs, kidneys, and brain regions (Hippocampus) were harvested. Tissue sections were prepared and stained with hematoxylin and eosin (H&E) to evaluate morphological integrity and pathological changes. Blood samples were collected at the time of euthanasia for routine hematological and biochemical analysis. Complete blood count (CBC) and blood haemato-biochemical were performed to assess the systemic impact of the drug intervention.

### **Behavioral experiments**

Prior to group assignment and A $\beta$ 1–42 oligomer injection (Day 0), all animals underwent comprehensive behavioral screening to ensure baseline equivalence. Open field test was conducted to assess general locomotor activity and anxiety-like behavior. Additionally, swimming capability was evaluated to ensure comparable motor function before water maze training. Only animals showing normal behavioral parameters were selected for the study and randomly assigned to experimental groups.

Behavioral tests were performed on each group of mice after 14 days of drug intervention.

#### **Open field test**

The open field test was performed to evaluate general locomotor activity and anxiety-related behavior. Mice were placed in a square arena, and their movement was tracked over a set period (300 s). Parameters such as distance traveled and time spent in the center versus near the walls were measured. Grid crossings were quantified by counting the number of times a mouse intersected the floor grid lines demarcated into equal-sized squares throughout the open field arena. Each intersection was considered a 'crossing', and the total number of crossings was recorded for the duration of the test. Grid crossing levels were categorized based on the frequency of crossings, with specific thresholds set for low, medium, and high levels of activity. These thresholds were determined empirically based on the distribution of crossings across all test subjects.

#### **Morris water maze**

The Morris water maze was employed to assess spatial learning and memory in mice. The experimental setup consisted of a circular pool where a platform was submerged just below the water surface. The pool was conceptually divided into four quadrants labeled in a clockwise sequence, with Quadrant 1 at the top-left and Quadrant 4 at the bottom-left, where the platform was positioned. Over a 5-day acquisition phase, mice were trained for 120 s per trial to locate this hidden platform. Each trial was initiated from varying starting points to ensure learning was not biased by the starting position. Escape latencies, the time taken by the mice to find and climb onto the submerged platform, were recorded daily to gauge learning progress. On the final day, a probe trial was conducted to evaluate spatial memory retention, where the platform was removed, and the time spent in the platform quadrant was recorded. To quantify spatial navigation efficiency, we calculated the ratio of the time each mouse spent heading directly toward the platform's location to the total time of the trial. This ratio served as an index of navigational precision and memory

recall for the platform's position. Additionally, enrichment scores were derived to represent the proclivity of mice to explore specific quadrants. The scores reflected the frequency at which different mouse groups visited each quadrant, providing a comparative measure of spatial preference, particularly noting the targeted quadrant housing the submerged platform. This analysis allowed us to infer the retention of spatial memory across various treatment groups.

#### **Y maze spontaneous alternation test**

The three arms of the labeled maze are A, B and C. Let the behavior software successfully connect with the Y maze camera and adjust the resolution to fully capture the mice in the maze. Place the test animal on the distal end of the arm labeled A, facing the center of the maze, and gently grasp the base of the tail. Leave the test room. The mice were allowed to explore the maze freely for 8 min. Mice were removed from the maze and returned to their original cages. Clean all walls and floors of the maze before moving on to the next animal. After completion of the experiment and testing of all designated mice, all mice were returned to their home cages in the holding room. Calculate the percentage alternation.

#### **Western blot analysis**

Protein concentrations in the brain homogenates were determined using the Bradford assay. Equal amounts of protein were loaded onto SDS-PAGE gels for separation and subsequently transferred onto PVDF membranes. The membranes were blocked and incubated with primary antibodies targeting A $\beta$ , NLRP3, Caspase-1, GSDMD-NT, IL-18 and IL-1 $\beta$ . GAPDH was used as a loading control. Appropriate HRP-conjugated secondary antibodies were applied, and the protein bands were visualized using enhanced chemiluminescence. Band intensities were quantified using densitometry.

#### **Elisa analysis**

The levels of NLRP3, Caspase-1, GSDMD-NT, IL-18, IL-1 $\beta$ , and A $\beta$  were quantified using enzyme-linked immunosorbent assays (ELISA). The assays were performed according to the manufacturer's protocols. Briefly, the respective capture antibodies for NLRP3, Caspase-1, GSDMD-NT, IL-18, IL-1 $\beta$ , and A $\beta$  were coated onto 96-well plates and incubated overnight at 4 °C. After blocking with 5% BSA in PBS for 1 h, the supernatants or cell lysates were added to the wells and incubated for 2 h at room temperature. Following extensive washing, the plates were incubated with biotinylated detection antibodies for 1 h at room temperature, followed by the addition

of HRP-conjugated streptavidin for 30 min. After the final wash, the substrate solution was added to each well, and the reaction was allowed to develop for 15 min. The absorbance was measured at 450 nm using a microplate reader. The concentrations of the analytes were determined using standard curves generated with recombinant proteins.

### Electron microscopy

For ultrastructural analysis, striatal samples were fixed, dehydrated, and embedded in resin. Ultrathin sections were cut and stained with uranyl acetate and lead citrate before examination under a transmission electron microscope.

### Immunofluorescence for ACS, caspase-1, GFAP, Iba-1, A $\beta$ and Th-T

Immunofluorescence staining was performed on hippocampus sections to detect ACS, Caspase-1, GFAP, Iba-1, A $\beta$  and Th-T. After blocking, sections were incubated with primary antibodies specific to each protein, followed by fluorescently labeled secondary antibodies. Fluorescence was detected using a confocal microscope, allowing for the localization and quantification of these proteins within the hippocampus tissue.

### Golgi-cox staining

Golgi-Cox staining of the hippocampus tissue was performed using the FD Rapid GolgiStain™ Kit (FD NeuroTechnologies, Hangzhou, China) following the manufacturer's protocol. Initially, the entire brain was immersed in the staining solution at room temperature for 14 days, shielded from light. Following this, the brain underwent a 3-day dehydration process at 4 °C in the staining solution. Coronal slices of the brain, each 100  $\mu$ m thick, were then prepared using a vibrating microtome (Leica, GER). These slices were placed in a chromogenic solution and allowed to develop color for 10 min at room temperature. Images of the PFC pyramidal neurons were captured using a microscope equipped with a 100 $\times$  objective lens (Olympus BX61, JPN).

### Supplementary Information

The online version contains supplementary material available at <https://doi.org/10.1186/s12951-025-03263-8>.

Supplementary material 1

### Author contributions

Jing Ma: Writing—original draft, Funding acquisition, Conceptualization. Yu Tian: Investigation. Chengzhong Du: Software. Yang Zhu: Data curation. Wen Huang: Visualization. Chenyu Ding: Formal analysis. Penghui Wei:

Methodology. Xuehan Yi: Project administration. Zhangya Lin: Writing—review & editing, Funding acquisition. Wenhua Fang: Funding acquisition.

### Funding

This work was supported by Neurological Disease Medical Center-Neurosurgery "double high" construction project scientific research project climbing project (2023YSJYX-PD-4); Natural Science Foundation of Fujian Province (2023J01664); Technology Platform Construction Project of Fujian Province (2021Y2001) and Technology Platform Construction Project of Fujian Province (2020Y2003).

### Data availability

Data is provided within the manuscript or supplementary information files.

### Declarations

#### Ethic approval and consent to participate

This research follows the process in accordance with ethical standards promulgated by the ethics committee of Fujian Medical University, approved by the Ethics Committee of Fujian Medical University (approval number: 1ACUC FJMU2022-0608).

#### Competing interest

The authors declare no competing interests.

#### Author details

<sup>1</sup>Department of Neurosurgery, Neurosurgery Research Institute, The First Affiliated Hospital, Fujian Medical University, Fuzhou 350005, Fujian, China. <sup>2</sup>Department of Neurosurgery, National Regional Medical Center, Binhai Campus of the First Affiliated Hospital, Fujian Medical University, Fuzhou 350212, Fujian, China. <sup>3</sup>Fujian Provincial Institutes of Brain Disorders and Brain Sciences, The First Affiliated Hospital, Fujian Medical University, Fuzhou 350005, Fujian, China. <sup>4</sup>Department of Otolaryngology Head and Neck Surgery, Fujian Medical University Union Hospital, Fuzhou 350001, Fujian, China.

Received: 17 December 2024 Accepted: 20 February 2025

Published online: 06 March 2025

### References

- Matej R, Tesar A, Rusina R. Alzheimer's disease and other neurodegenerative dementias in comorbidity: a clinical and neuropathological overview. *Clin Biochem*. 2019;73:26–31.
- Phillips ML, Stage EC, Lane KA, Gao S, Risacher SL, Goukasian N, Saykin AJ, Carrillo MC, Dickerson BC, Rabinovici GD, Apostolova LG. Neurodegenerative patterns of cognitive clusters of early-onset Alzheimer's disease subjects: evidence for disease heterogeneity. *Dement Geriatr Cogn Disord*. 2019;48:131–42.
- Skillbäck T, Farahmand BY, Rosén C, Mattsson N, Nägga K, Kilander L, Religa D, Wimo A, Winblad B, Schott JM, et al. Cerebrospinal fluid tau and amyloid- $\beta$ 1-42 in patients with dementia. *Brain*. 2015;138:2716–31.
- Davidson K, Bano M, Parker D, Osmulski P, Gaczynska M, Pickering AM:  $\beta$ -Amyloid impairs Proteasome structure and function. Proteasome activation mitigates amyloid induced toxicity and cognitive deficits. *bioRxiv* 2024.
- Revi M. Alzheimer's disease therapeutic approaches. *Adv Exp Med Biol*. 2020;1195:105–16.
- Zhu Y, Niu X, Wu T, Cheng J, Zou J, Pan Y, Tian Y, Wei H, Ding C, Lin Y, et al. Metal-phenolic nanocatalyst rewires metabolic vulnerability for catalytically amplified ferroptosis. *Chem Eng J*. 2024;485:150126.
- Zhang Y, Zhao Y, Zhang J, Yang G. Mechanisms of NLRP3 inflammasome activation: its role in the treatment of Alzheimer's disease. *Neurochem Res*. 2020;45:2560–72.
- Seoane PI, Lee B, Hoyle C, Yu S, Lopez-Castejon G, Lowe M, Brough D. The NLRP3-inflammasome as a sensor of organelle dysfunction. *J Cell Biol*. 2020. <https://doi.org/10.1083/jcb.202006194>.
- Zheng R, Yan Y, Dai S, Ruan Y, Chen Y, Hu C, Lin X, Xue N, Song Z, Liu Y, et al. ASC specks exacerbate  $\alpha$ -synuclein pathology via amplifying NLRP3 inflammasome activities. *J Neuroinflammation*. 2023;20:26.

10. Liang Y, Song P, Chen W, Xie X, Luo R, Su J, Zhu Y, Xu J, Liu R, Zhu P, et al. Inhibition of caspase-1 ameliorates ischemia-associated blood-brain barrier dysfunction and integrity by suppressing pyroptosis activation. *Front Cell Neurosci.* 2020;14:540669.
11. Saresella M, Marventano I, Piancone F, La Rosa F, Galimberti D, Fenoglio C, Scarpini E, Clerici M. IL-33 and its decoy sST2 in patients with Alzheimer's disease and mild cognitive impairment. *J Neuroinflammation.* 2020;17:174.
12. Xu H, Chen J, Chen P, Li W, Shao J, Hong S, Wang Y, Chen L, Luo W, Liang G. Costunolide covalently targets NACHT domain of NLRP3 to inhibit inflammasome activation and alleviate NLRP3-driven inflammatory diseases. *Acta Pharm Sin B.* 2023;13:678–93.
13. Xu Y, Zhou Z, Deng N, Fu K, Zhu C, Hong Q, Shen Y, Liu S, Zhang Y. Molecular insights of nanozymes from design to catalytic mechanism. *Sci China Chem.* 2023;66:1318–35.
14. Zhu Y, Ding C, Fang W, Li T, Yan L, Tian Y, Huang W, Wei P, Ma J, Lin X, et al. Metal-polyphenol self-assembled nanodots for NIR-II fluorescence imaging-guided chemodynamic/photodynamic therapy-amplified ferroptosis. *Acta Biomater.* 2024;185:361–70.
15. Guo Q, Xu X, Lai X, Duan J, Yan D, Wang D. Antigen/adjuvant-free liposome induces adjuvant effects for enhancing cancer immunotherapy. In: *Exploration.* Wiley Online Library: Hoboken; 2024. p. 20230115.
16. Qin Z, Li Y, Gu N. Progress in applications of prussian blue nanoparticles in biomedicine. *Adv Healthc Mater.* 2018;7:e1800347.
17. Gao X, Wang Q, Cheng C, Lin S, Lin T, Liu C, Han X. The application of prussian blue nanoparticles in tumor diagnosis and treatment. *Sensors.* 2020;20:6905.
18. Grancharova T, Simeonova S, Plicheva B, Zagorchev P. Gold nanoparticles in Parkinson's disease therapy: a focus on plant-based green synthesis. *Cureus.* 2024;16:e54671.
19. Tracy GC, Huang KY, Hong YT, Ding S, Noblet HA, Lim KH, Kim EC, Chung HJ, Kong H. Intracerebral nanoparticle transport facilitated by Alzheimer pathology and age. *Nano Lett.* 2023. <https://doi.org/10.1021/acs.nanolett.3c03222>.
20. Li D, Liu M, Li W, Fu Q, Wang L, Lai E, Zhao W, Zhang K. Synthesis of prussian blue nanoparticles and their antibacterial, antiinflammation and antitumor applications. *Pharmaceuticals.* 2022. <https://doi.org/10.3390/ph15070769>.
21. Singh R, Singh S. Redox-dependent catalase mimetic cerium oxide-based nanozyme protect human hepatic cells from 3-AT induced acatalasemia. *Colloids Surf B Biointerfaces.* 2019;175:625–35.
22. Li N, Yang H, Wang M, Lü S, Zhang Y, Long M. Ligand-specific binding forces of LFA-1 and Mac-1 in neutrophil adhesion and crawling. *Mol Biol Cell.* 2018;29:408–18.
23. Wesenhausen KEJ, Tijms BM, Boonkamp L, Hoede PL, Goossens J, Dewit N, Scheltens P, Vanmechelen E, Visser PJ, Teunissen CE. P-tau subgroups in AD relate to distinct amyloid production and synaptic integrity profiles. *Alzheimers Res Ther.* 2022;14:95.
24. Meng G, Liu J, Lin S, Guo Z, Xu L. Microcystin-LR-caused ROS generation involved in p38 activation and tau hyperphosphorylation in neuroendocrine (PC12) cells. *Environ Toxicol.* 2015;30:366–74.
25. Zhang Y, Rong H, Zhang FX, Wu K, Mu L, Meng J, Xiao B, Zamponi GW, Shi Y. A membrane potential- and calpain-dependent reversal of caspase-1 inhibition regulates canonical NLRP3 inflammasome. *Cell Rep.* 2018;24:2356–2369. e2355.
26. Flores J, Noël A, Fillion ML, LeBlanc AC. Therapeutic potential of Nlrp1 inflammasome, caspase-1, or caspase-6 against Alzheimer disease cognitive impairment. *Cell Death Differ.* 2022;29:657–69.
27. Li Y, Jiang Q. Uncoupled pyroptosis and IL-1 $\beta$  secretion downstream of inflammasome signaling. *Front Immunol.* 2023;14:1128358.
28. Zhu Y, Niu X, Ding C, Lin Y, Fang W, Yan L, Cheng J, Zou J, Tian Y, Wei H, et al. Carrier-free self-assembly nano-sonosensitizers for sonodynamic-amplified cuproptosis-ferroptosis in glioblastoma therapy. *Adv Sci.* 2024. <https://doi.org/10.1002/advs.202402516>.
29. Moretti R, Pansiot J, Bettati D, Strazielle N, Ghersi-Egea JF, Damante G, Fleiss B, Titomanlio L, Gressens P. Blood-brain barrier dysfunction in disorders of the developing brain. *Front Neurosci.* 2015;9:40.
30. Mulberg AE, Cripps T. Global harmonization of pediatric drug development: critical for progress for developing safe and effective therapeutic agents for children. *Curr Ther Res Clin Exp.* 2019;90:109–12.
31. Rehman M, Madni A, Shi D, Ihsan A, Tahir N, Chang KR, Javed I, Webster TJ. Enhanced blood brain barrier permeability and glioblastoma cell targeting via thermoresponsive lipid nanoparticles. *Nanoscale.* 2017;9:15434–40.
32. Mursaleen L, Noble B, Somavarapu S, Zariwala MG. Micellar nanocarriers of hydroxytyrosol are protective against Parkinson's related oxidative stress in an in vitro hCMEC/D3-SH-SY5Y co-culture system. *Antioxidants.* 2021;10:887.
33. Pervin M, Unno K, Nakagawa A, Takahashi Y, Iguchi K, Yamamoto H, Hoshino M, Hara A, Takagaki A, Nanjo F, et al. Blood brain barrier permeability of (-)-epigallocatechin gallate, its proliferation-enhancing activity of human neuroblastoma SH-SY5Y cells, and its preventive effect on age-related cognitive dysfunction in mice. *Biochem Biophys Res.* 2017;9:180–6.
34. Zhu H, Li B, Chan CY, Ling BLQ, Tor J, Oh XY, Jiang W, Ye E, Li Z, Loh XJ. Advances in Single-component inorganic nanostructures for photoacoustic imaging guided photothermal therapy. *Adv Drug Deliv Rev.* 2023;192:114644.
35. Usenovic M, Niroomand S, Drolet RE, Yao L, Gaspar RC, Hatcher NG, Schachter J, Renger JJ, Parmentier-Batteur S. Internalized tau oligomers cause neurodegeneration by inducing accumulation of pathogenic tau in human neurons derived from induced pluripotent stem cells. *J Neurosci.* 2015;35:14234–50.
36. Hashimoto S, Matsuba Y, Kamano N, Mihira N, Sahara N, Takano J, Muramatsu SI, Saido TC, Saito T. Tau binding protein CAPON induces tau aggregation and neurodegeneration. *Nat Commun.* 2019;10:2394.
37. Wang G, Jin S, Liu J, Li X, Dai P, Wang Y, Hou SX. A neuron-immune circuit regulates neurodegeneration in the hindbrain and spinal cord of Arf1-ablated mice. *Natl Sci Rev.* 2023;10:nwad222.
38. Choi S, Kim D, Kam TI, Yun S, Kim S, Park H, Hwang H, Pletnikova O, Troncoso JC, Dawson VL, et al. Lysosomal enzyme glucocerebrosidase protects against A $\beta$ 1-42 oligomer-induced neurotoxicity. *PLoS ONE.* 2015;10:e0143854.
39. Tao X, Zhang R, Wang L, Li X, Gong W. Luteolin and exercise combination therapy ameliorates amyloid- $\beta$ 1-42 oligomers-induced cognitive impairment in AD mice by mediating neuroinflammation and autophagy. *J Alzheimers Dis.* 2023;92:195–208.
40. Suzuki Y, Nakamoto C, Watanabe-Iida I, Watanabe M, Takeuchi T, Sasaoka T, Abe M, Sakimura K. Quantitative analysis of NMDA receptor subunits proteins in mouse brain. *Neurochem Int.* 2023;165:105517.
41. Huang W, Tian Y, Ma J, Wei P, Du C, Zhang X, Chen F, Lin Y, Zhu Y, Kang D. Neutrophil membrane-based biomimetic metal-polyphenol self-assembled nanozyme for the targeting treatment of early brain injury following subarachnoid hemorrhage. *Chem Eng J.* 2024;498:155643.
42. Zhu Y, Liao Y, Zou J, Cheng J, Pan Y, Lin L, Chen X. Engineering single-atom nanozymes for catalytic biomedical applications. *Small.* 2023;19:e2300750.
43. Wu S, Hu L, Lin J, Li K, Ye S, Zhu S, Liu Z. Excretion of amyloid- $\beta$  in the gastrointestinal tract and regulation by the gut microbiota. *J Alzheimers Dis.* 2022;90:1153–62.
44. Miller LVC, Papa G, Vaysburd M, Cheng S, Sweeney PW, Smith A, Franco C, Katsinelos T, Huang M, Sanford SAI, et al. Co-opting templated aggregation to degrade pathogenic tau assemblies and improve motor function. *Cell.* 2024. <https://doi.org/10.1016/j.cell.2024.08.024>.

## Publisher's Note

Springer Nature remains neutral with regard to jurisdictional claims in published maps and institutional affiliations.